Title
Modeling of Branching and Plant Growth via a Modified Elastica

Author
Tresierras, Timothy Nicholas

Publication Date
2009

Peer reviewed|Thesis/dissertation

Modeling of Branching and Plant Growth via a Modified Elastica

by

Timothy Nicholas Tresierras

A dissertation submitted in partial satisfaction of the
requirements for the degree of
Doctor of Philosophy

in

Engineering-Mechanical Engineering

in the

GRADUATE DIVISION
of the
UNIVERSITY OF CALIFORNIA, BERKELEY

Committee in charge:
Professor Oliver O'Reilly, Chair
Professor Panayiotis Papadopoulos
Professor Alexandre Bayen

Fall 2009

Modeling of Branching and Plant Growth via a Modified Elastica

Abstract

Modeling of Branching and Plant Growth via a Modified Elastica

by

Timothy Nicholas Tresierras
Doctor of Philosophy in Engineering-Mechanical Engineering

University of California, Berkeley

Professor Oliver O'Reilly, Chair

One of the most remarkable sites in nature is the branched structure of plants. The branching enables the plant to increase its capability to photosynthesize and to support its flowering structures. The shape of a plant's branches depend on a wide range of factors, some of which vary with the growth stage of the plant.

To accommodate the factors featured in plant growth, Euler's original theory is modified to include the effects of lateral accretion, tip growth, and residual (or growth) stresses. As a result, a theory of deformable rods featuring time-varying intrinsic curvature, flexural rigidity, moment of inertia, mass density, and length is developed. The resulting theory is supplemented by a novel growth evolution equation. This equation is used to control the evolution of the intrinsic curvature in response to changes in flexural rigidity and moment of inertia. We also introduce a novel control curvature to address the deficiency in accommodating residual (growth) stresses that are inherent in any rod theory. The novel growth law is illustrated with a range of examples. It is also compared and related to earlier published works on plant stem growth modeling.

Another contribution of the thesis is the development of a graphical technique to determine the shape of branched structures. Here, a plant with multiple stem bifurcations is considered and the graphical technique is used to explain the multiplicity of static configurations that the plant can display. We close the dissertation with an outline of future work on the modeling of plant growth and branching.

To Christopher Reid Neilsen,

who first sparked my imagination.

&

To Hector Robert Tresierras,

who told me,

“nothing to it, but to do it.”

Contents

List of Figures

List of Tables

Acknowledgments

I would like to thank various people, not necessarily on the level of importance, but in the order in which they made this degree possible. However, I will begin with my father and mother, Hector and Gloria Tresierras, who happen to be the first chronologically and highest in importance that I would like to thank. They taught me to remember that who I am as a person will always outweigh any achievement. I have dedicated this work to my lifelong friend Reid Neilsen and send out my heart felt appreciation to the extended Neilsen family for their influence in stimulating my imagination and introducing me to a love for science ("I really loved my Zoobooks!").

My graduate school guardian angel, Beatriz Lopez-Flores, has been my number one supporter during my graduate career and has opened up so many channels of opportunity, I am eternally grateful. In addition, I would like to thank the support of the entire Center for Underrepresented Engineering Students (CUES) staff for their involvement in enriching not only my graduate experience, but countless others. I can never forget the fact that Professor Roberto Horowitz was pretty much the person who gave me the "thumbs up" and let me into the graduate program. I thank him for giving me a chance at Berkeley and defending me during my Qualification Exam. I am truly grateful for choosing him to be the chair of my Qualifying Exam committee. A special thanks goes out to Robert M. Nordlund, my former employer, who gave me sound advise of which I will never forget during a time when I was unsure of my graduate career. Since my first class with him as my instructor to the my last days at Berkeley with him as my advisor, Professor Oliver O'Reilly has been an excellent teacher, mentor, and friend. His undisputed classification as a professor that truly cares is the reason why I stayed at Berkeley.

I would also like to thank my girlfriend, Sara Rothan, and her family for allowing me to grow as a person and providing me with solitude and a retreat from my academics. This reminds me, I would also like acknowledge the Richmond Bridge, whose long and boring corridor allowed my mind to wonder to such a degree that nearly every innovative idea I have contributed in this body of work began as a kernel of thought on that bridge. Also of foremost importance, making my graduate experience memorable, was my core group of friends and surf crew, Dan Prull, Sara Felix, Giovanni Gonzalez, Shantisa Norman, and Ben Fine.

In the realm of seemingly endless support, I also would like to thank my brother Mario Tresierras for his advice and always helping me at a moments notice when I was in a financial pickle.

Also, you cannot find one ME alumnus that doesn't own a debt of thanks to both Pat Giddings and Donna Craig for always being available to help out and basically being human search engines for any question pitched their way. Finally, I would like to thank Professor Panos Papadopoulos and Professor Alex Bayen for being on my dissertation committee, the students in Professor O'Reilly's lab for reading over my dissertation, and Patch Kessler for giving me some of the most amazing feedback on my thesis.

Chapter 1

Introduction

The vines and stems of wooden and non-wooden plants display remarkable feats of movement and growth at time-scales that are much slower than the human eye can perceive. Circumnutation, twining, and gravitropism are among the various dynamic phenomena we have yet to fully understand [3, 4]. One of the most remarkable sites in nature, however, is the branched structure of plants. The shape of a plant's branches depend on a wide range of factors, some of which vary with the growth stage of the plant. Branching enables the plant to increase its capability to photosynthesize and to support its flowering structures, which typically manifests in divergent and discontinuous plant configurations, such as the segmented growth shown in Fig. 1.1.

Figure 1.1: *Shown above are several segmented branches of Schlumbergera truncata, also known as Crab Cactus or Christmas Cactus. An isolated segment and the centerline of the plant is outlined in the right branch.*

According to a survey by Kurth [5], there are numerous models for predicting growth and for predicting plant architecture. These models, based on botanical knowledge, range from macro-scale simulations that use stochastic processes as a theoretical basis to mirco-scale models that focus on isolated processes such as water conduction and transpiration. Due to the complexity of plants, most models have yet to fully integrate external growth

factors like light and water availability, hydraulics, mechanical stability, gas exchange and carbon allocation, response to mechanical obstacles, and physiological constraints.

Our motivation is to develop a simplified mechanical model that accounts for various plant growth phenomena for the purpose of mid-scale analysis. There are few mechanics-based algorithms for predicting the growth and branching of plants. Several works have pioneered the use of the dynamic theory of slender rod-like bodies for plant growth. The work of Silk, Wang, and Cleland [6] uses Euler's elastica to quantify the mechanics of the rice panicle. In Fig. 1.2 we show an example of the configurational structure of the rice panicle. The combined works of [3, 7, 8] outline a variety of problems ranging from the

Figure 1.2: *A rice panicle, Oryza sativa, provides a motivational example of the various simple plant forms we would like to model with a simplified rod theory. Silk et al. [1] makes extensive observational analysis on the rice panicle using a simple beam model.*

mechanics of climbing and twinning plants to intrinsic curvature's role in tendril perversion.

Like most of these previous works based on a mechanical theory, we focus in this work on slender rod-like bodies and their branchings. In a recent paper by Faruk Senan, O'Reilly, and Tresierras [9], we modeled plant growth and branching using a rod-based theory featuring Euler's elastica. This work extended the works of Silk et al. [1] and Goreily et al. [10], who recently used a modified theory of the elastica to model the "morphoelasticity" of plant tendrils. The novel features of the model developed in [9] include a simple evolution equation for the flexural rigidity and intrinsic curvature and the use of an intermediate (growth) configuration, while additionally establishing an open-ended path toward more elaborate rod theories which accommodate nonplanar motions, transverse shear, and

torsion.[1]

Using a rod theory as a model for plants, we can pick a set of points along a curve in the body as the centerline of the rod. When the plant experiences growth we find that material points are continually being added to this centerline, while the lateral dimensions of the rod are also changing. These changes are termed *growth*: the lateral (or secondary) growth is known as cambial growth, and the tip (or primary) growth is due to the activity of stem apical meristem cells. Additionally, a *remodeling* or *morphogenesis* can occur and be considered as a set of changes in the constitutive properties of the body such as a change in the modulus of elasticity. The change in parameters in time is known as an *evolution*.

To accommodate the factors featured in plant growth, Euler's original theory is modified in Chapter 2 to include the effects of lateral accretion, tip growth, and residual (or growth) stresses. As a result, a theory of deformable rods featuring time-varying intrinsic curvature, flexural rigidity, moment of inertia, mass density, and length is developed. The resulting theory is supplemented by a novel growth evolution equation in Chapter 3. This equation is used to control the evolution of the intrinsic curvature in response to changes in flexural rigidity and moment of inertia. The resulting evolution equation is more realistic than the one used in [9] because it can accommodate rapid tip growth and lateral surface accretion. We also introduce a novel control curvature to address the deficiency in accommodating the residual (growth) stresses that are inherent in any rod theory. The novel growth law is illustrated with a range of examples. It is also compared and related to earlier published works on plant stem growth modeling.

Another contribution of the thesis is developed in Chapter 4, where a graphical technique to determine the shape of branch structures is developed. In Chapter 5, a plant with multiple stem bifurcations is considered and the graphical technique is used to explain the multiplicity of static configurations that the plant can display. We close the dissertation with an outline of future work on the modeling of plant growth and branching.

[1]Details on more elaborate rod theories can be found in Antman [11, 12], Green and Naghdi [13], and Rubin [14].

Chapter 2

A Simple Rod-Based Model for Plant Growth

2.1 Introduction and Motivation

Euler's theory of the elastica [15] can be the basis for a tractable plant model [9] and is the simplest nonlinear theory of a deformable rod which features resistance to bending and extension. Euler and Jakob Bernoulli (1744) developed the theory for elastic lines, which yielded solutions known as the *elastica curve* (also simply referred to as the *elastica*) and studied buckling. Later, elastica theory was generalized by F. and E. Cosserat (1907) into a geometric theory with intrinsic directions at each point. We present our work in a framework similar to those used in continuum theories of growth. Our treatment of the balance laws for the elastica is strongly influenced by the works of Green, Naghdi and their coworkers (see [13, 16, 14] and references therein). Although our modified elastica can capture a rich assortment of plant growth characteristics, the model, unlike three-dimensional continuum theories, cannot be used to estimate residual stresses which are known to accompany many growth processes in biology.

To use a rod theory to model a growing plant stem, three configurations are needed. In addition to the familiar present and reference configurations, a growth configuration is defined. The curvature of the rod in this configuration is the intrinsic curvature κ^g. We find that the present configuration relaxes to the growth configuration when all the applied forces and moments are removed. We further adapt the elastica by including a time varying intrinsic curvature κ^g [10] and time varying stiffness modulus D.

The agreement between the elastica curves in Fig. 2.1, and the rice panicle in Fig. 1.2 suggests that the elastica is an appropriate model for plants.

2.2 Configurations and Material Curves

To capture the kinematics of the elastica, we consider a reference configuration $\mathcal{L}^0$ where the centerline is straight and the cross-sections are normal to this centerline. The centerline is a material curve $\mathcal{C}$. We use a coordinate ξ to parameterize this curve; we denote the end

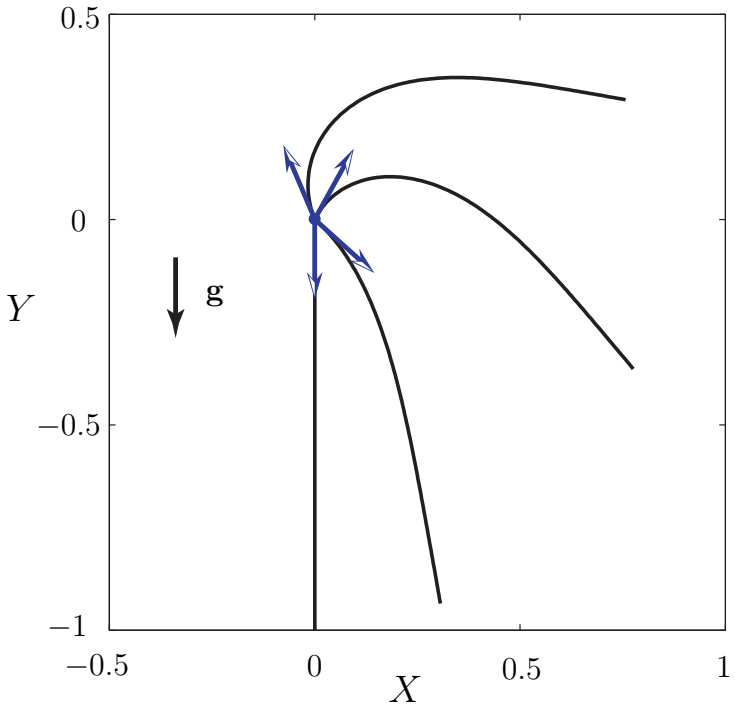

Figure 2.1: *Four instances of a cantilevered elastica are simulated for four different initial tangent vectors at the base (the arrows at the origin). The elasticae represent identical homogeneous constant cross-section rods of unit length that are free of any contact force or moment at the free tip.*

points of $\mathcal{C}$ by $\xi = \xi_A$ and $\xi = \xi_B$. To model the cross-sectional features, each point on $\mathcal{C}$ is endowed with an area A, a moment of area I and a mass density ρ_0. As time t evolves, tip growth and mass deposition and accretion occur, so A, I, ρ_0 are functions of t and ξ. In addition, ξ_A and ξ_B are functions of time. We also anticipate that some constitutive remodeling of the elastica will occur. This remodeling will be reflected in changes to its constitutive equations.

We consider the reference configuration $\mathcal{L}^0$ to be embedded on a plane in $\mathbb{E}^3$. The unit normal to this plane is a constant vector $\mathbf{E}_3$. The position vector of a material point on $\mathcal{C}$, the centerline of the reference configuration, is given by $\mathbf{r}_0(\xi, t)$ and we choose our origin O such that

$$\mathbf{r}_0(\xi, t) = r_0(\xi, t)\,\mathbf{E}_2 + \mathbf{c} \tag{2.1}$$

where $\mathbf{c}$ is a constant vector and $\{\mathbf{E}_1, \mathbf{E}_2, \mathbf{E}_3\}$ is a set of fixed right-handed Cartesian basis vectors. The coordinate ξ is the arc-length coordinate for $\mathcal{C}$ in $\mathcal{L}^0$. We assume the existence of a continuous segment of material points in $\mathcal{L}^0$.

The present configuration $\mathcal{L}$ of the elastica is assumed to be embedded on the same plane in $\mathbb{E}^3$. The present configuration shows the actual state of the elastica at time t. The position of a point on $\mathcal{C}$ in the present configuration is given by the vector $\mathbf{r} = \mathbf{r}(\xi, t)$.

A motion χ of the elastica is a mapping from $\mathcal{L}^0$ to $\mathcal{L}$. This motion encompasses the

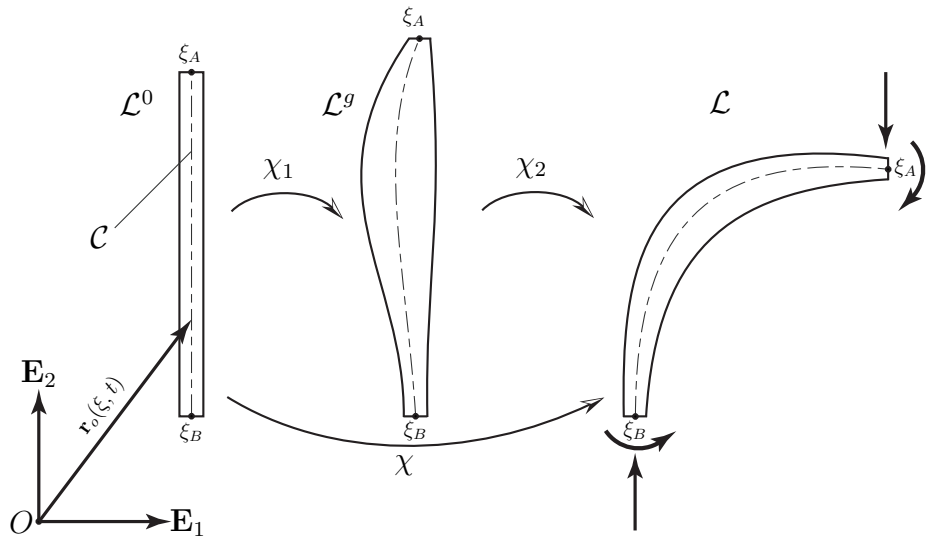

Figure 2.2: *The elastica is represented by the rod centerline in three configurations, $\mathcal{L}^0$, $\mathcal{L}^g$, and $\mathcal{L}$. Each centerline is a material curve $\mathcal{C}$ parameterized by the reference configuration's arc-length parameter ξ.*

response of the elastica due to changes in mass, remodeling and the effects of impressed forces and moments. It turns out that χ is not particularly useful. Instead, it is convenient to construct an intermediate (or growth) configuration $\mathcal{L}^g$. The configuration $\mathcal{L}^g$ can be attained from $\mathcal{L}$ by removing the external forces and external moments on the elastica. That is, $\mathcal{L}^g$ is the unloaded configuration (at time t) of $\mathcal{L}$. We define the position of a point on $\mathcal{C}$ in the growth configuration by the vector $\mathbf{r}^g = \mathbf{r}^g(\xi, t)$. Due to the changes in area, inertia, mass density and internal constitution, the configuration $\mathcal{L}^g$ also evolves in time. Further, as illustrated in Figure 2.2, two motions χ_1 and χ_2 can be defined which relate $\mathcal{L}^0$ to $\mathcal{L}^g$ and $\mathcal{L}^g$ to $\mathcal{L}$, respectively.

Through out this work we assume an inextensible elastica (i.e., unity stretch):

$$\mu = \frac{\partial s}{\partial \xi} = 1, \tag{2.2}$$

where s is an arc-length parameter in the present configuration. This constraint allows us to neglect the use of the reference configuration, and to parameterize the growth and present configuration with the coordinate s.

2.3 Kinematics

Prior to presenting the balance laws we present definitions of various kinematic quantities. The elastica is constrained to a plane and so it is torsion free. A practical right-handed orthonormal basis for the centerline of the elastica is $\left[\mathbf{e}_t(s), \mathbf{e}_n(s), \mathbf{E}_3\right]$, where $\mathbf{e}_t(s)$ is the

unit tangent vector and $\mathbf{e}_n(s)$ is the corresponding unit normal vector. The vectors $\mathbf{e}_t(s)$ and $\mathbf{e}_n(s)$ are defined as follows:

$$\begin{aligned} \frac{\partial \mathbf{r}}{\partial s} = \mathbf{e}_t = &\quad \cos\big(\theta(s)\big)\mathbf{E}_1 + \sin\big(\theta(s)\big)\mathbf{E}_2, \\ \frac{1}{\kappa}\frac{\partial \mathbf{e}_t}{\partial s} = \mathbf{e}_n = &-\sin\big(\theta(s)\big)\mathbf{E}_1 + \cos\big(\theta(s)\big)\mathbf{E}_2, \end{aligned} \tag{2.3}$$

where κ is the curvature[1] in the present configuration and θ is the angle between the tangent vector $\mathbf{e}_t$ and the horizontal unit vector $\mathbf{E}_1$. We note that in the present configuration $\mathcal{L}$,

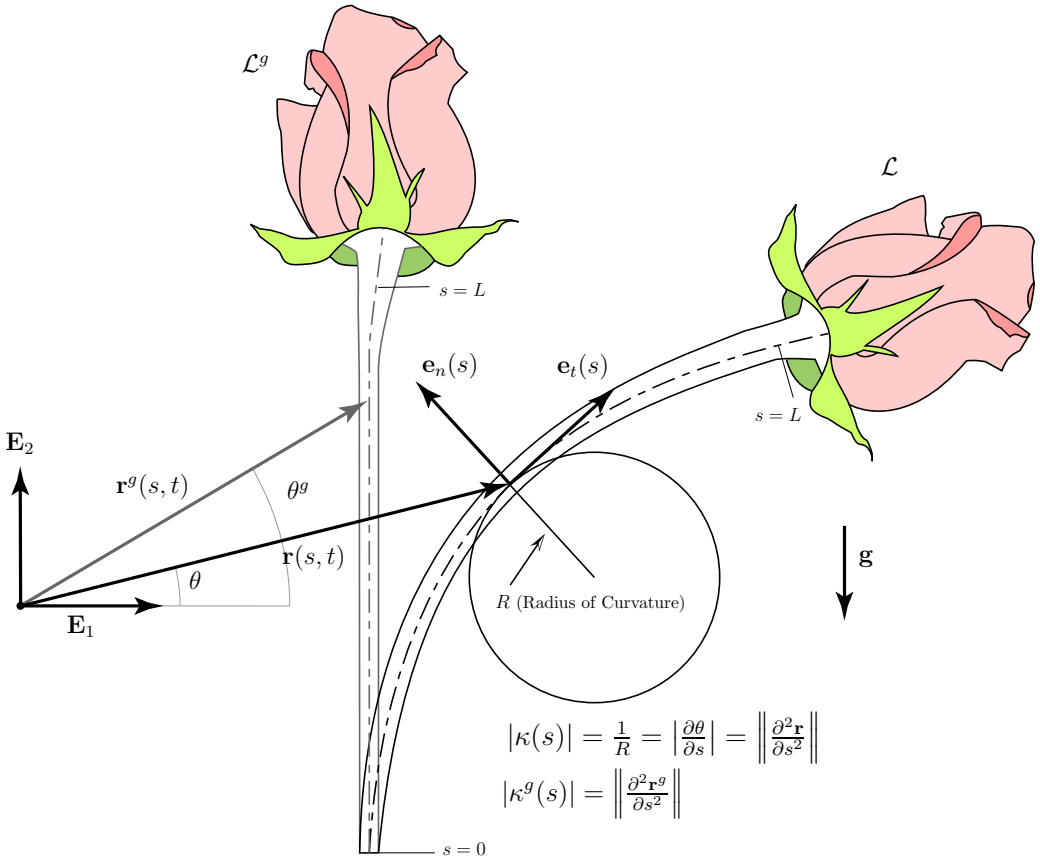

Figure 2.3: *The centerline of a rose stem as modeled by the elastica. The configuration $\mathcal{L}$ is loaded by a self-weight body force induced by gravity, $\mathbf{g} = -g\mathbf{E}_2$. The centerline of the unloaded configuration $\mathcal{L}^g$ shows the intrinsic (growth) curvature κ^g. This centerline is not necessarily straight. The inverse of the absolute value of curvature is the radius of curvature.*

$$\kappa = \frac{\partial \theta}{\partial s}. \tag{2.4}$$

[1]We have made use of a *signed* curvature as opposed to classical treatments of differential geometry that represent curvature as a positive value.

Likewise, the curvature of the rod in the growth configuration $\mathcal{L}^g$ is called the *intrinsic curvature* κ^g and is defined by

$$\kappa^g = \frac{\partial \theta^g}{\partial s}. \tag{2.5}$$

The difference in curvature between the present and growth configurations is denoted

$$\nu = \kappa - \kappa^g, \tag{2.6}$$

and is called the *relative strain* (or *strain*). Figure 2.3 shows the basis $[\mathbf{e}_t(s), \mathbf{e}_n(s), \mathbf{E}_3]$, the curvature κ's relation to the radius of curvature, and how the present configuration $\mathcal{L}$ relaxes to the growth configuration $\mathcal{L}^g$ when all forces and moments are removed.

2.4 Forces and Moments

The contact force $\mathbf{n}$ and the contact moment $\mathbf{m}$ are usually supplemented by the assigned force $\rho\mathbf{f}$ and assigned moment $\mathbf{m}_a$. However, in this dissertation we assume $\mathbf{m}_a = \mathbf{0}$. In Fig. 2.4 we illustrate the contact force, contact moment, and assigned force relative to a thin cross-sectional slice of a rod. Using (2.3), the contact force $\mathbf{n}$ in the rod is decomposed

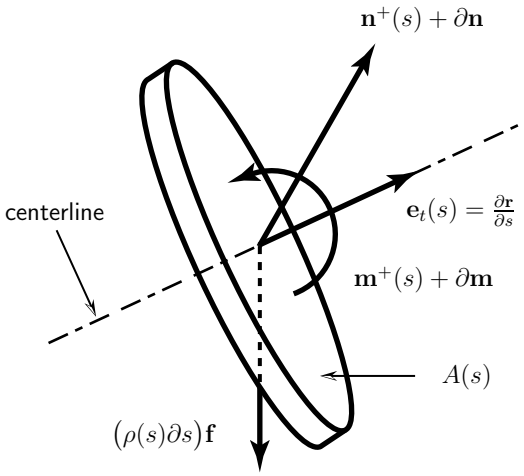

Figure 2.4: *An example of the force and moment balance on an infinitesimally thin cross-sectional slice of a continuous interval of a rod. The contact force* $\mathbf{n}^-(s)$ *and contact moment* $\mathbf{m}^-(s)$ *are not shown.*

as

$$\mathbf{n} = n_t\mathbf{e}_t + n_s\mathbf{e}_n, \tag{2.7}$$

where n_t and n_s are called the tension and shear forces, respectively.

We introduce point supplies of linear momentum $\mathbf{F}$ and angular momentum relative to the origin $\mathbf{M}_O$. Arc-length coordinates of a point s at which these supplies act is denoted $s = \gamma$. We denote by $\mathbf{M}$ the resultant moment of these supplies about $\mathbf{r}(\gamma, t)$,

$$\mathbf{M} = \mathbf{M}_O - \mathbf{r}\,(\gamma, t) \times \mathbf{F}. \tag{2.8}$$

The objects $\mathbf{M}$, $\mathbf{M}_O$, and $\mathbf{F}$ all live in the present configuration $\mathcal{L}$.

2.5 Branching and Discontinuities

In this section we use jump conditions to address rod discontinuities. Discontinuities occur at points called nodes. As illustrated in Fig. 2.5, a node can be

- A point at which the rod centerline is only C^0 (i.e., not continuously differentiable).
- A bifurcation point in which a single branch splits into two or more branches.
- A point where a singular force $\mathbf{F}$ or moment $\mathbf{M}$ is applied.

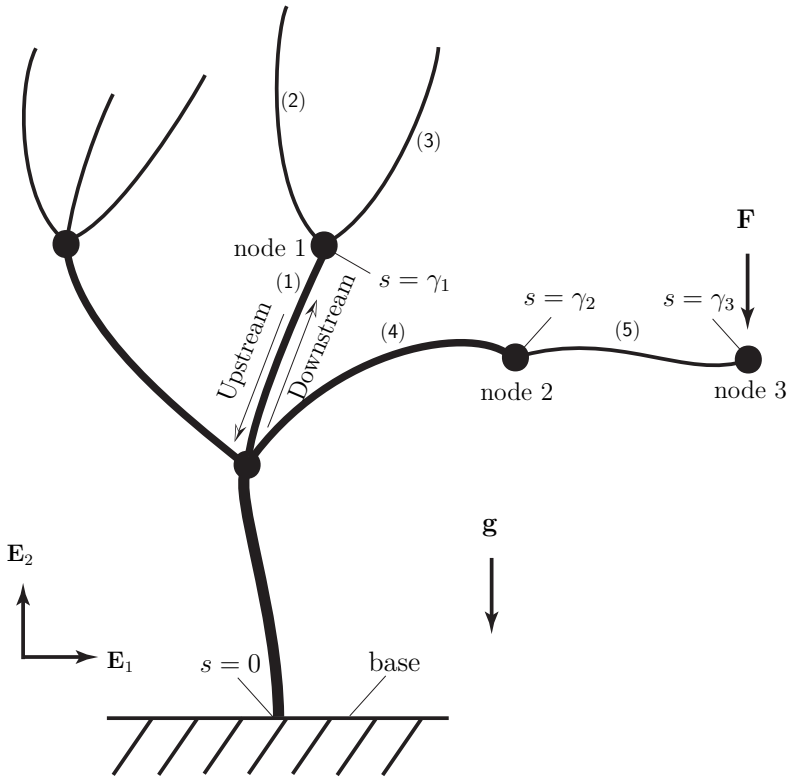

Figure 2.5: *Upstream and downstream directions are labeled and shown by arrows. Various branches are labeled in parenthesis. The labeled nodes represent three general discontinuities that we focus on in this dissertation.*

Jump conditions allow us to account for multiple branches, tip growth, and singular loads (e.g., a piece of fruit).[2]

[2]In the following, we use the term *branch* or *stem* in a general sense to describe a continuous segment of a configuration that terminates at either a nodal point or a free end and can be used synonymously with the term *rod*.

Figure 2.5 shows a system of rods representing a multi-branch structure under the influence of gravity. Moving along any particular rod, we refer to *upstream* as the direction in which moving along the rod through the nodes brings one closer to an anchored base. Likewise, *downstream* is moving in the opposite direction (i.e., toward the branch tips). At a particular node, we call a branch leading toward the upstream direction an *upstream branch*, and we call a branch leading toward the downstream direction a *downstream branch*. We observe that plants, have a *contractive flow* in the upstream direction, i.e., the number of upstream branches at a node is always equal to or less than the number of downstream branches at a node (See Fig. 2.5). The image is reminiscent of the forked pattern in a river delta, is why we refer to upstream as the direction in which the branching system contracts.

To make use of jump conditions, we need to define upstream and downstream limits of functions. For an arbitrary function $\mathcal{X}(s)$, the jump condition, $[\![\mathcal{X}]\!]$, denotes the change of the function $\mathcal{X}(s)$ across a node $s = \gamma$:

$$\mathcal{X}^{\pm} = \lim_{\sigma \to 0} \mathcal{X}(s \pm \sigma), \quad [\![\mathcal{X}]\!] = \mathcal{X}^{+} - \mathcal{X}^{-}, \tag{2.9}$$

where $\sigma > 0$, $\mathcal{X}^{+}$ is the value of the function just downstream of a node $s = \gamma$, and $\mathcal{X}^{-}$ is the value of the function just upstream of a node $s = \gamma$.

2.5.1 Generalized Branching Points

For nodes at the tip of a branch, we set $\mathcal{X}^{+} = 0$. For node 2 and node 3 in Fig. 2.5 we can use the previous definition of the operation $[\![\cdot]\!]$. However, for branching points, such as node 1 in Fig. 2.5, we must generalize $[\![\cdot]\!]$.

Imagine a continuous branch $\mathcal{L}_1$ bifurcating into two branches $\mathcal{L}_2$ and $\mathcal{L}_3$. We parameterize these configurations by the arc-length coordinates s_1, s_2, and s_3, respectively, and we choose these parameterizations such that at the branching point $s_1 = s_2 = s_3 = \gamma$. Further, on $\mathcal{L}_1$, $s_1 \leq \gamma$, whereas on $\mathcal{L}_2$, $s_2 \geq \gamma$, and on $\mathcal{L}_3$, $s_3 \geq \gamma$. Given an arbitrary function $\mathcal{X}$ defined on all three branches $\big(\mathcal{X} = \mathcal{X}_i(s_i)$ on branch $\mathcal{L}_i\big)$, we define

$$[\![\mathcal{X}]\!]_3 = \lim_{\sigma \to 0} \big(\mathcal{X}_3(s_3 = \gamma + \sigma) + \mathcal{X}_2(s_2 = \gamma + \sigma) - \mathcal{X}_1(s_1 = \gamma - \sigma)\big), \tag{2.10}$$

where $\sigma > 0$ and the subscript 3 on $[\![\cdot]\!]_3$ indicates that three functions are involved in the calculation.[3]

2.6 Balance Laws and Jump Conditions

We now recalled the balance laws for the modified elastica, postulated in [9]. In departure from [9], we assume inextensibility.

We endow material curve with a mass density per unit length of ρ. This density is a product of the cross-sectional area A and the mass density per unit volume ρ^{*}. As a result,

[3]It should be clear from this definition how $[\![\cdot]\!]$ is a special case of $[\![\cdot]\!]_3$ and how the latter can be extended to branching points featuring the bifurcation of four or more branches.

ρ can change if mass is added in such a way as to increase A. At each point on the curve we also assign a moment of inertia I. We note that the three scalar fields ρ, A and I are functions of s and t.

A theory that accommodates plant growth needs to include discrete and continuous sources of mass. The discrete sources of mass are active during tip growth, while the continuous sources are active during secondary growth. This secondary growth results in a thickening of the plant stem. In a one-dimensional theory, the addition of mass causes the mass per unit length and the inertia change. Our balance laws are more general than those which appear in the standard literature on rod theories. In the subsequent sections we consider a segment of the material curve bounded by the material points $s = s_1$ and $s = s_2$.

2.6.1 Balance of Inertia

For an arbitrary rod segment, we postulate the following inertial balance laws:

$$\begin{aligned} \frac{d}{dt}\int_{s_1}^{s_2} \rho ds - \underbrace{[\rho \dot{s}]_{s_1}^{s_2}} &= \int_{s_1}^{s_2} \left(\rho m^0 + M^0\,\delta(s-\gamma)\right)\, ds, \\ \frac{d}{dt}\int_{s_1}^{s_2} \rho I ds - \underbrace{[\rho I \dot{s}]_{s_1}^{s_2}} &= \int_{s_1}^{s_2} \left(\rho m^I + M^I\,\delta(s-\gamma)\right)\, ds, \end{aligned} \tag{2.11}$$

where $\delta(\cdot)$ is the Dirac delta distribution, ρm^0 is a distributed mass source, ρm^I is a distributed inertia source, M^0 is a singular supply of mass, and M^I is a singular supply of moment of inertia. The underbraced terms in (2.11) arise because material can be added to the segment in question. That is, $\dot{s}_{1,2} \neq 0$. Related terms appear in the other balance laws we present.

The balance laws (2.11) are equivalent to

$$\dot{\rho} = \rho m^0, \qquad \frac{d}{dt}(\rho I) = \rho m^I, \tag{2.12}$$

and the corresponding jump conditions

$$[\![\rho]\!]\,\dot{\gamma} = M^0, \qquad [\![\rho I]\!]\,\dot{\gamma} = M^I. \tag{2.13}$$

2.6.2 Balance of Momentum

Motivated by (2.12), we define a derivative which captures the time-rate of change of a kinematical variable due to changes in ρ and ρI:

$$\overset{m}{\overline{\rho f}} = \rho m^0 f, \qquad \overset{m}{\overline{\rho I f}} = \rho m^I f, \tag{2.14}$$

where $f = f(s,t)$. Thus,

$$\overset{m}{\overline{\rho \dot{\mathbf{r}}}} = \rho m^0 \dot{\mathbf{r}}, \qquad \overset{m}{\overline{\rho I \dot{\theta}}} = \rho m^I \dot{\theta}. \tag{2.15}$$

We now consider an arbitrary length of the material curve $\mathcal{C}$ which is bounded by the coordinates s_1 and s_2. To accommodate growth, we allow s_1 and s_2 to be time-dependent. The balance of linear momentum is

$$\frac{d}{dt}\int_{s_1}^{s_2}\rho\dot{\mathbf{r}}ds-[\rho\dot{\mathbf{r}}\dot{s}]_{s_1}^{s_2}-\int_{s_1}^{s_2}\overset{m}{\overline{\rho\dot{\mathbf{r}}}}\,ds=[\mathbf{n}]_{s_1}^{s_2}+\int_{s_1}^{s_2}\rho\mathbf{f}\,ds+\int_{s_1}^{s_2}\mathbf{F}\,\delta(s-\gamma)\,ds. \tag{2.16}$$

The balance of angular momentum is

$$\begin{aligned}\frac{d}{dt}\int_{s_1}^{s_2}\mathbf{H}_O ds-[\mathbf{H}_O\dot{s}]_{s_1}^{s_2}-\int_{s_1}^{s_2}\overset{m}{\mathbf{H}}_O\,ds &= [\mathbf{r}\times\mathbf{n}+\mathbf{m}]_{s_1}^{s_2}\\ &\quad+\int_{s_1}^{s_2}(\mathbf{r}\times\mathbf{f}+\mathbf{m}_a)\,\rho ds\\ &\quad+\int_{s_1}^{s_2}\mathbf{M}_O\,\delta(s-\gamma)\,ds,\end{aligned} \tag{2.17}$$

where the angular momentum $\mathbf{H}_O$ relative to the origin O is defined as

$$\mathbf{H}_O=\rho\mathbf{r}\times\dot{\mathbf{r}}+\rho I\dot{\theta}\mathbf{E}_3, \tag{2.18}$$

which is specified per unit length of s.

The local forms of the balance laws are obtained from (2.16) and (2.17) with the help of (2.12):

$$\begin{aligned}\rho\ddot{\mathbf{r}}&=\rho\mathbf{f}+\frac{\partial\mathbf{n}}{\partial s},\\ \rho I\ddot{\theta}\mathbf{E}_3&=\rho\mathbf{m}_a+\frac{\partial\mathbf{r}}{\partial s}\times\mathbf{n}+\frac{\partial\mathbf{m}}{\partial s}.\end{aligned} \tag{2.19}$$

From the balance laws (2.16) and (2.17), we also find that the following jump conditions must hold at $s=\gamma(t)$:

$$\begin{aligned}[\![\mathbf{n}+\dot{\gamma}\rho\dot{\mathbf{r}}]\!]+\mathbf{F}&=\mathbf{0},\\ \left[\!\!\left[\mathbf{m}+\dot{\gamma}\rho I\dot{\theta}\mathbf{E}_3\right]\!\!\right]+\mathbf{M}&=\mathbf{0}.\end{aligned} \tag{2.20}$$

It can be shown that (2.19) and (2.20) are collectively equivalent to (2.16) and (2.17).

2.7 Equations of Motion for an Elastica

Our model captures two forms of movement. *Growth-related* movement is due to time-related changes in material properties, while *reactionary* movement is due to the time rate of change components in the equations of motion. The time scales of these forms of movement can differ by several orders of magnitude.

We are only concerned with growth related movement, and so we model a plant with static equations of motion. Under this restriction, the balance laws[4] take the following form,

$$\rho\mathbf{f} + \frac{\partial \mathbf{n}}{\partial s} = \mathbf{0}, \quad \frac{\partial \mathbf{m}}{\partial s} + \frac{\partial \mathbf{r}}{\partial s} \times \mathbf{n} = \mathbf{0}, \tag{2.21}$$

where s is arc-length, $\rho\mathbf{f}$ is the body force per unit length, $\mathbf{n}$ is the contact force, $\mathbf{m}$ is the contact moment, and $\mathbf{r}$ is the position vector. The jump conditions at a static discontinuity, which respectively correspond to the previous equations, are

$$[\![\mathbf{n}]\!] + \mathbf{F} = \mathbf{0}, \qquad [\![\mathbf{r} \times \mathbf{n} + \mathbf{m}]\!] + \mathbf{M}_O = \mathbf{0}, \tag{2.22}$$

where $\mathbf{F}$ is a singular force and $\mathbf{M}_O$ is a singular moment relative to the origin. Additionally, we assume that the position vector at any dislocation point $\mathbf{r}(\gamma)$ is always continuous.

In order to capture intrinsic curvature, we prescribe the following simple free energy function $\rho\psi$:

$$\rho\psi = \frac{1}{2} D(\kappa - \kappa^g)^2, \tag{2.23}$$

where D is the bending stiffness (flexural rigidity) of the rod. As in [9], the local form of the balance of energy leads to the following constitutive equation for $\mathbf{m}$:

$$\begin{aligned} \mathbf{m} &= D\left(\frac{\partial \theta}{\partial s} - \frac{\partial \theta_g}{\partial s}\right)\mathbf{E}_3 \\ &= D(\kappa - \kappa^g)\mathbf{E}_3 \\ &= D\nu\,\mathbf{E}_3. \end{aligned} \tag{2.24}$$

2.7.1 A Discontinuity Equivalence

As shown in Fig. 2.6, there is an equivalent approach to the treatment of a branching discontinuity and a discontinuity due to a singular force and moment. In Fig. 2.6 the leading end branch of a three-branch configuration is reduced to an equivalent two-branch configuration with a singular force $\mathbf{F}$ and singular moment $\mathbf{M}$ imposed at the tip.

A singular moment relative to the node at $s = \gamma$ is given by

$$\mathbf{M} = \mathbf{M}_O - \mathbf{r}(\gamma) \times \mathbf{F}.$$

Because $\mathbf{r}(\gamma)$ is continuous, the nodal jump equations $(2.22)_{1,2}$ expand into the following:

$$\begin{aligned} \mathbf{n}^+ - \mathbf{n}^- + \mathbf{F} &= \mathbf{0}, \\ \mathbf{m}^+ - \mathbf{m}^- + \mathbf{M} &= \mathbf{0}. \end{aligned} \tag{2.25}$$

[4]Equation $(2.21)_1$ is the local balance of linear momentum and equation $(2.21)_2$ is the local balance of angular momentum. We omit showing the local form of the balance of energy. However, the local form of the balance laws are identically satisfied by our constitutive equation for $\mathbf{m}$.

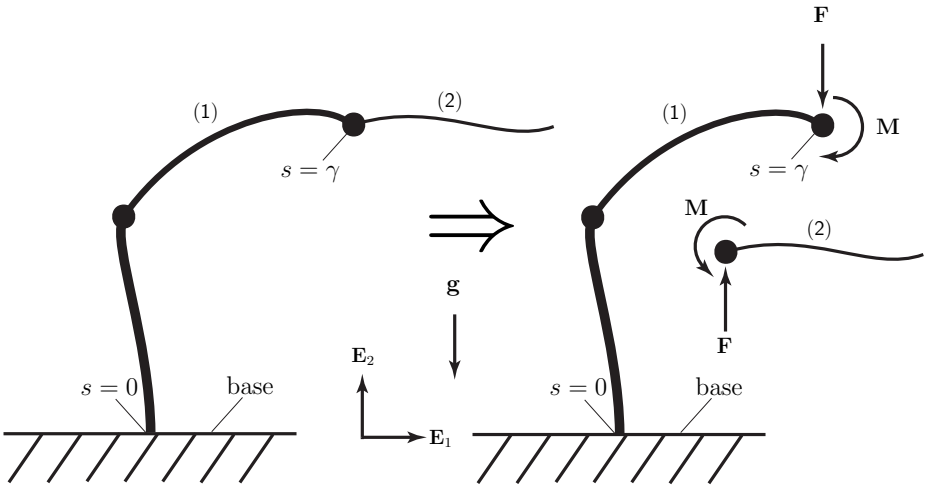

Figure 2.6: *The loading and torque at the node $s = \gamma$ due to branch (2) on the branched configuration on the left is equivalently represented by the singular force and moment imposed on the node at the tip of the branched configuration on the right.*

Initially accounting for branch (2) in Fig. 2.6 at the node $s = \gamma$, we let $\mathbf{F} = \mathbf{0}$ and $\mathbf{M} = \mathbf{0}$ and find that

$$\begin{aligned} \mathbf{n}^- &= \mathbf{n}^+, \\ \mathbf{m}^- &= \mathbf{m}^+. \end{aligned} \tag{2.26}$$

However, if we assume that the downstream branch is reduced to an equivelent singular force and moment imposed at the node $s = \gamma$, then $\mathbf{n}^+ = \mathbf{0}$, and $\mathbf{m}^+ = \mathbf{0}$, and $(2.25)_{1,2}$ becomes

$$\begin{aligned} \mathbf{n}^- &= \mathbf{F}, \\ \mathbf{m}^- &= \mathbf{M}, \end{aligned} \tag{2.27}$$

where $\mathbf{F}$ and $\mathbf{M}$ can after be expressed as function of the angle θ at $s = \gamma$ in the upstream branch (1).

The equivalent approaches expressed by $(2.26)_{1,2}$ and $(2.27)_{1,2}$ are used in Chapter 5. From the previous example we find that an arbitrary number of branches at a node can be accommodated and that the equivalent reduction can continue until we arrive at a single base branch.

2.8 Single Stem ODEs

In plant biology models, it is important to account for the geometric taper that is often present in branches. It is equally important to attempt to capture the non-homogeneous nature of constitutive parameters along the branches.

In order to properly generalize the equations of motion for our use as a plant model, we first consider that the force and moment at the free end, $s = L$, of a single cantilevered branch are zero. At the base of this single branch, $s = 0$, the vertical force is comprised of the branch weight and there is no horizontal force component. We extend this concept to configurations with several branches. Every every node is subject to a vertical contact force $\mathbf{n}$ which is equal to the total weight of the branch(es) downstream of the node. It follows from Section 2.7.1 that the vertical contact force $\mathbf{n}$ is equivalent to a vertical singular force $\mathbf{F}$.

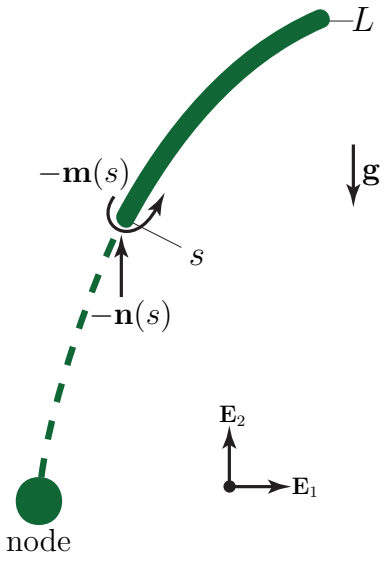

Figure 2.7: *The union of the dashed and solid line represents a branch hanging under its self-weight that is free at one end and connected to a node at another end. The integration interval between an arbitrary value of the arc-length parameters s and L is represented by the solid line. The value of the integral in (2.28) is the weight of the branch between an arbitrary on the of the rod and the tip $s = L$.*

As exemplified in Fig. 2.7, we integrate $(2.21)_1$ from an arbitrary point on the branch to the tip $s = L$:

$$\mathbf{n}(L) - \mathbf{n}(s) = g \int_L^s -\rho(\bar{s})\mathrm{d}\bar{s}\, \mathbf{E}_2, \tag{2.28}$$

where gravity $\mathbf{g} = -g\mathbf{E}_2$ has been prescribed, L is the total length of a branch segment, and ρ is a function of the arc-length parameter s. By defining the integral in the previous equation as

$$\mathcal{P} = \int_L^s -\rho(\bar{s})\mathrm{d}\bar{s}, \tag{2.29}$$

we simplify (2.28) as follows

$$\mathbf{n}(L) - \mathbf{n}(s) = \mathcal{P} g \mathbf{E}_2. \tag{2.30}$$

The body force prescription is weight in the vertical $(-\mathbf{E}_2)$ direction, and so the additional contact forces due to other branches will be strictly vertical. Thus, $\mathbf{n}(L)$ is given by

$$\mathbf{n}(L) = n_{L_2}\mathbf{E}_2. \tag{2.31}$$

We define the vertical component n_{L_2} by a downward force $\mathbf{F} = -n_l\mathbf{E}_2$ imposed at the tip of the branch. The following equations arise from (2.30) for the similarly decomposed components of $\mathbf{n}(s) = n_1\mathbf{E}_1 + n_2\mathbf{E}_2$:

$$\begin{aligned} n_1 &= 0, \\ n_2 &= -(\mathcal{P}g + n_l). \end{aligned}$$

These forces can also be decomposed into tension, $n_t = \mathbf{n}(s)\cdot\mathbf{e}_t$ and shear, $n_s = \mathbf{n}(s)\cdot\mathbf{e}_n$ forces:

$$\begin{aligned} n_t &= -(\mathcal{P}g + n_l)\sin(\theta), \\ n_s &= -(\mathcal{P}g + n_l)\cos(\theta). \end{aligned} \tag{2.32}$$

Using $(2.21)_1$, $(2.21)_2$, (2.24) and (2.6) with the prescription that a gravitational force acts on the rod (i.e., $\mathbf{f} = -g\mathbf{E}_2$) and utilizing $(2.32)_2$, we arrive at the equations of motion,[5]

$$\begin{aligned} \theta' &= \nu + \kappa^g, \\ \nu' &= \left(\frac{\mathcal{P}g + n_l}{D(s,t)}\right)\cos(\theta) - \frac{D'(s,t)}{D(s,t)}\nu, \\ \mathcal{P}' &= -\rho(s,t), \end{aligned} \tag{2.33}$$

where $D(s,t)$ and $\rho(s,t)$ are prescribed functions of arc-length and time. The function κ^g will later be replaced by a temporal evolution equation.

Since the rod can be translated anywhere in the plane, the following equations,

$$\begin{aligned} X' &= \cos\theta(s), \\ Y' &= \sin\theta(s), \end{aligned} \tag{2.34}$$

which determine the position vector

$$\mathbf{r} = X\mathbf{E}_1 + Y\mathbf{E}_2 \tag{2.35}$$

in the plane, remain independent from the third-order system (2.33). Also, the most convenient boundary condition for the state $\mathcal{P}$ is

$$\mathcal{P}(L,t) = 0. \tag{2.36}$$

The additional boundary conditions for $(2.33)_{1,2}$ will be discussed in the following chapters.

The equations in (2.33) can also be derived using a variational method. This derivation is shown in Appendix A. The energy functional used in this method of derivation is exploited in Chapter 4.

[5]The prime $'$ indicates a partial derivative with respect to the parameter s.

2.8.1 The Special Case of ODEs for a Single Stem

If we assume that the modeled branch is homogeneous and has a constant cross-sectional area (i.e., the mass per unit length of the rod, ρ, and the bending stiffness D are constant), then by integrating $(2.21)_1$ from an arbitrary point on the branch to the tip $s = L$ we obtain

$$\mathbf{n}(L) - \mathbf{n}(s) = \rho g(L - s)\mathbf{E}_2. \tag{2.37}$$

As in the previous section we find a reduced order system:

$$\begin{aligned} \theta' &= \nu + \kappa^g, \\ \nu' &= \frac{1}{D}(\rho g(L - s) + n_l)\cos(\theta). \end{aligned} \tag{2.38}$$

This second-order system is used in numerous illustrative examples in Chapter 4.

Chapter 3

Growth

3.1 Introduction and Motivation

In addition to lateral and axial growth, plants can control their movement as they grow. The different types of plant movement are known as tropisms e.g., phototropism and gravitropism. Phototropism is movement influenced by light. Gravitropism (or geotropism) is a movement in a stem or root influenced by gravity. In particular, stems tend to experience negative gravitropism: growth opposite the direction of the pull of gravity [1]. In this chapter we use gravitropism to motivate a model of growth related movement.

Negative gravitropism can occur is several different ways. One of these is known as turning (or bending), and can be induced by the plant hormone auxin [17]. As illustrated

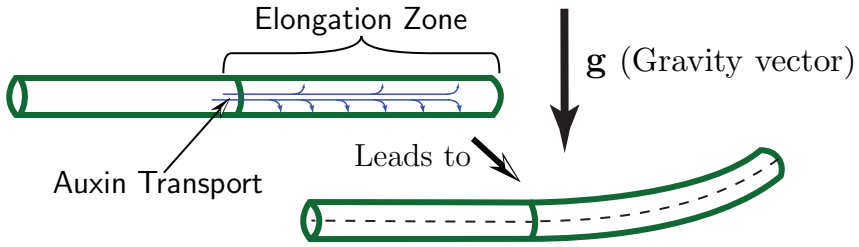

Figure 3.1: *The elongation zone, typically at the tip of a non-wooden stem, experiences a higher concentration of the plant hormone auxin at the stem underside. Compared to the topside of the stem, the higher concentration leads to faster cell expansion, resulting in an upward curvature in the elongation zone.*

in Fig. 3.1, the plant hormone becomes concentrated on the bottom side of the stem. A higher concentration promotes faster cell expansion (or *differential growth*) and induces an upward curvature. The prevalence of this mechanism varies from species to species. Most non-wooden plants rely on turning in the elongation zone at the tip of the growing stem.

Wooden stems in contrast tend to rely less on turning and instead have been observed to develop tension wood (or *residual growth stress*) on the upper-side of a branch in the secondary xylem [2], see Fig. 3.2. According to Malan [18], growth stresses are generated

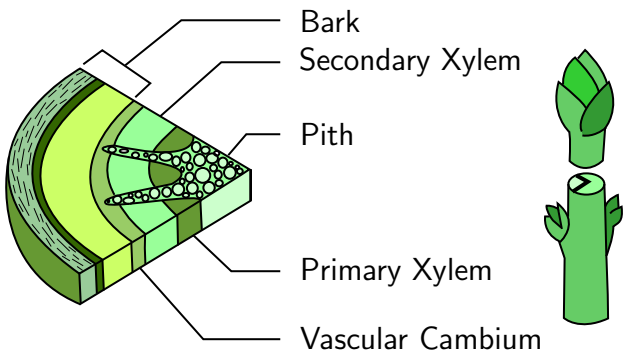

Figure 3.2: *A cross-section of a wooden stem showing the general location of the secondary xylem, where tension wood has been observed to develop on the upper-side of the non-vertical segments of a branch.*

within woody tissue as a result of the tendency of differentiating cells to contract during cell maturation. Layers of cells added to the stem are laid down in a state of tension, which has a cumulative effect of counterbalancing compressive forces. In other words, The tension wood prevents a downward collapse of the branch as additional torque is produced by the addition of mass during further primary and secondary growth.

3.2 Equations of Motion and Evolution

In general, a plant moves by changing its geometric and constitutive properties that constitute its configuration. We recall the equations of motion, (2.33) that were derived in Chapter 2,

$$\begin{aligned}\theta' &= \nu + \kappa^g(s,t),\\ \nu' &= \left(\frac{\mathcal{P}g + n_l}{D(s,t)}\right)\cos(\theta) - \frac{D'(s,t)}{D(s,t)}\nu,\\ \mathcal{P}' &= -\rho(s,t),\end{aligned}$$

based on a modified theory of Euler's inextensible elastica. Although the equations of motion are ODEs, the parameters can vary in time and along the arc-length s, which allows us to account for features such as stem taper, lateral accretion of material, plant morphogenesis, and remodeling. Jump conditions $(2.22)_{1,2}$ account for significant singular loads and moments at branching nodes, as well as tip growth. The model allows us to choose a simple constitutive equation (2.24), where $D = EI$ is again a bending stiffness parameter (where E is the modulus of elasticity, and I is the cross-sectional area moment of inertia). Again, κ is the curvature of the present configuration $\mathcal{L}$, and κ^g is the curvature of the growth configuration $\mathcal{L}^g$.[1]

[1]We sometimes use the symbol for curvature of a particular configuration to refer to the configuration e.g., "...the growth configuration κ^g...".

In this chapter we establish evolution equations that can be used in conjunction with the equations of motion to capture various growth phenomena in both wooden and non-wooden plants. The term *evolution* refers to the temporal change of a rod's constitutive parameters (e.g., D, ρ) and intrinsic curvature κ^g. We assume a relationship between the constitutive parameters and the intrinsic curvature. Furthermore, we assume that a positive rate of change in rigidity D independently influences the change in intrinsic curvature κ^g. However, we acknowledge that additional influences on the intrinsic curvature κ^g can be present. Our evolution equations account for this additional influence.

We initially consider two ways in which rigidity changes over time. The first is by a lateral accretion of material and the second is by a remodeling of the rod's constitutive properties. We usually treat stiffness D as one parameter. However, when we refer to *remodeling* we are implying that $\dot{E} > 0$ results in the temporal change in D. Likewise, when we refer to *accretion* we are implying that $\dot{I} > 0$ results in the temporal change in D. In the subsequent sections we address how the present and growth configurations are affected by a decrease in stiffness caused either by $\dot{E} < 0$ or by $\dot{I} < 0$.

3.3 Previous Works on Growth

In Faruh Senan et al. [9], a simple evolution equation for remodeling was established for an evolving growth configuration based on the assumption of a static present configuration. Figure 3.3 reproduces a simulation in [9] for a rod undergoing pure remodeling without lateral accretion or tip growth. The simulation shows a growth (intrinsic) configuration approaching the shape of the static present configuration as the stiffness parameter D increases over time due to constitutive remodeling. The simulation captures a common phenomenon in plants that was observed by Goriely et al. [10].

The evolution equation in [9] is based on the assumption of a constant moment in time, $\dot{\mathbf{m}} = \mathbf{0}$, along the arc-length and fails to capture realistic growth movement when lateral accretion or tip growth become significant. In other words, the evolution law fails when the change in moment along the arc-length is significant due to the addition of material. Without applying an evolution law, Figure 3.4 shows the effect of a uniform rod hanging lower as the tip is allowed to grow in time. Applying the simple evolution law and allowing the stiffness parameter D of the initial rod to increase in time due to constitutive remodeling, Figure 3.4 shows that the rod tends to hang lower than the rod that does not undergo remodeling. If the simulation is allowed to continue, the growing rod with the simple evolution experiences a quicker collapse. This is contrary to what we see happen in nature. According to Yamamoto and Yoshida [2], wooden plants rely on significant asymmetric residual stresses in their non-vertical limbs to support an expansive system of branches. Clearly, the residual stress has not been accounted for in the simple evolution law used in [9].

Yamamoto and Yoshida demonstrate the importance of residual stress by showing that the tip of a growing stem can only grow outward and upward to within ceratin limits before eventually hanging lower to the ground. As noted by Yamamoto and Yoshida in [2], this is in contrast to some researchers who believe that a plant stem can continually grow upward

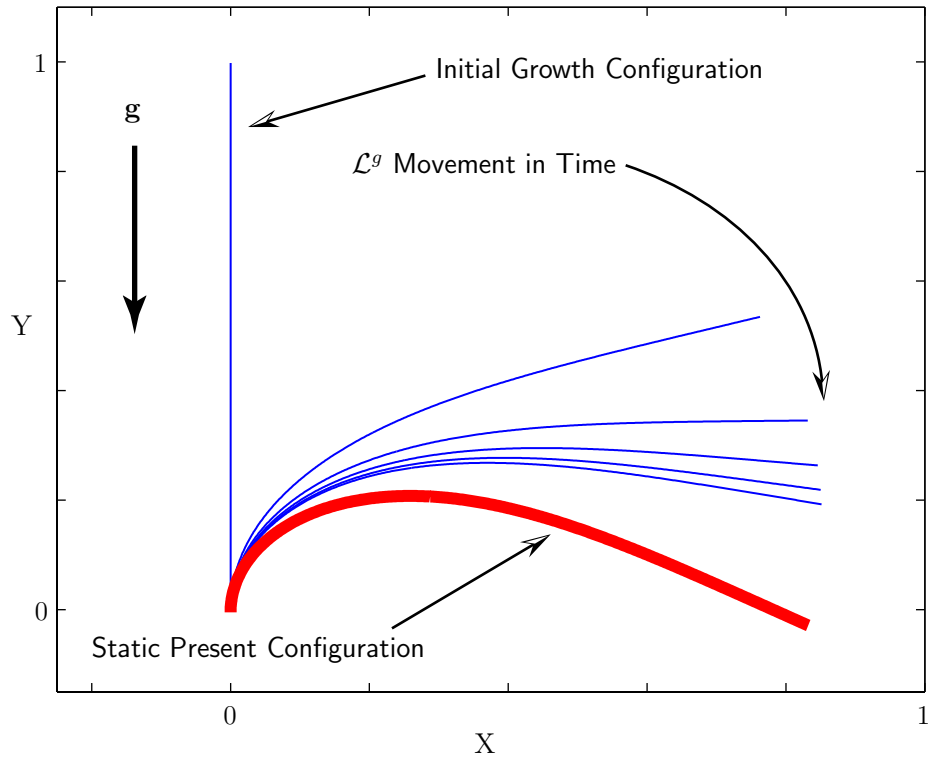

Figure 3.3: *The thick curve represents the static present configuration $\mathcal{L}$ of a uniform constant cross-section rod with rigidity that is increasing with time (i.e., remodeling). The thin curves represents progressive instances of the rod's growth configuration $\mathcal{L}^g$ in time. Initially straight, the growth configuration approaches the static present configuration. The stiffness parameter D evolves according to a prescribed first order ODE step response.*

by having a preferred angle of growth at the tip of the stem. We agree with Yamamoto and Yoshida on the importance of residual growth stress.

Figure 3.5 shows simulations[2] of the progressive tip growth of a stem with the elongation zone (at the tip) having a preferred angle $\theta^p = 30°$, where the tip growth angle is defined relative to the horizontal. The thicker stem in the figure shows the point at which additional tip growth does not lead to any significant outward and/or upward growth. The simulations in Fig. 3.5 duplicate results by Yamamoto and Yoshida [2], but do so using different numerical methods. Based on these results they deduced the importance of the development of growth stress in wooden branches, which leads to a more expansive branched configurations as compared to non-wooden plants. Residual growth stresses are typically insignificant in non-wooden plants because the process of turning in the elongation zone at the tip of a stem is typically enough to obtain a negative tropism or upward movement.

Relative to the model established in Chapter 2, the process of growing a limb with a preferred angle at the tip, (Fig. 3.5), is the same as growing an arbitrarily shaped initial

[2]The details of the simulation are discussed in Section 3.6.3.

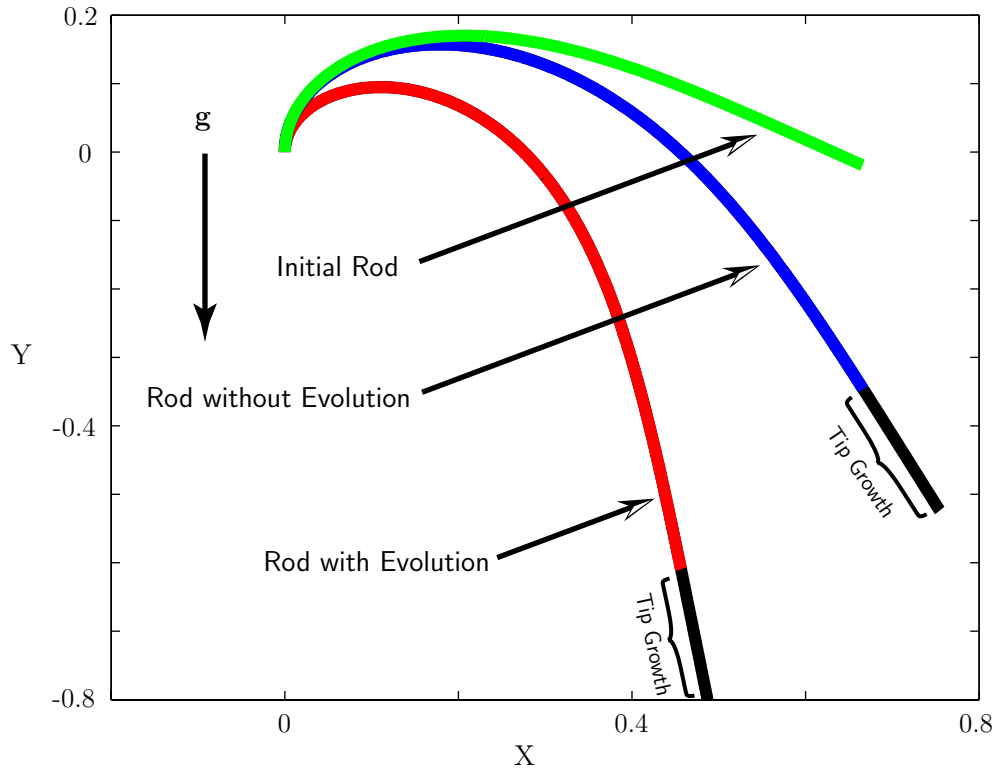

Figure 3.4: *The same initial rod in Fig. 3.3 is now allowed to have the tip of the rod grow in time. The rod undergoing constitutive remodeling hangs lower over time compared to the rod that does not have an evolution law imposed on it.*

growth configuration $\mathcal{L}_o^g$ whose curvature κ^g remains constant in time. In [2], Yamamoto and Yoshida devise a numerical growth model which makes implicit use of a growth configuration and a posteriori method for accounting for the effects of residual growth stress on branch curvature.

3.4 A Continuous Evolution Equation for κ^g

In this section we present a continuous evolution equation for κ^g. In the previous section we discussed various problems with the simple evolution equation in our earlier work [9]. The evolution law that we discuss here solves these problems by accounting for residual stresses and allowing for rapid lateral accretion and tip growth.

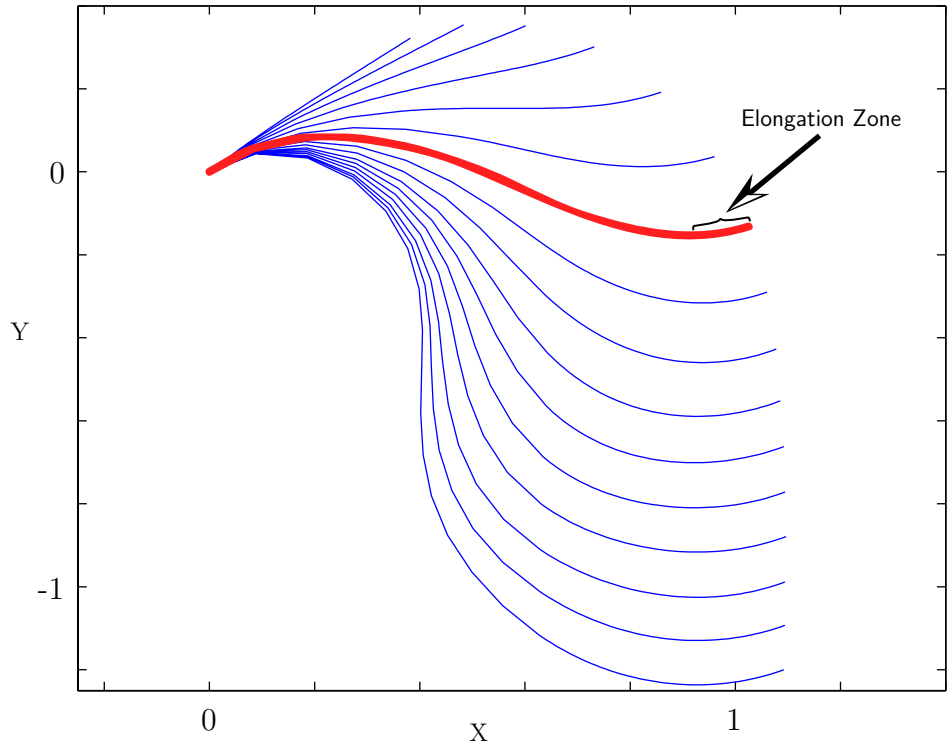

Figure 3.5: *Progressive configurations depicting tip growth of a branch with a preferred angle $\theta^p = 30°$ of tip growth, where the tip growth angle is defined relative to the horizontal. The branch is homogeneous, with a uniform cross-section. The sinusoidal shape of the thick branch can be observed in mature maritime pine branches [2].*

3.4.1 Postulated Form of the General Evolution Equation for κ^g

We postulate the following continuous evolution equation for κ^g when $\dot{E} \geq 0$ and $\dot{I} \geq 0$,

$$\kappa^g(s,t) = \frac{D_o\kappa_o^g + \int_{t_0}^{t}\left[\dot{D}(s,\tau)\big(\kappa(s,\tau)+\kappa^c(s,\tau)\big)\right]\mathrm{d}\tau + \int_{t_0}^{t}\left(D(s,\tau)\dot{\kappa}_I^g(s,\tau)\right)\mathrm{d}\tau}{D(s,t)}, \tag{3.1}$$

where $D_o = D(s,t_o)$, $\kappa_o^g = \kappa^g(s,t_o)$, and $\kappa^c(s,t) = 0$ when $\dot{I} = 0$. Under special conditions, when

$$\dot{\kappa}_I^g = \dot{\overline{\kappa+\kappa^c}}, \tag{3.2}$$

we can evaluate the integral in (3.1) to obtain

$$\kappa^g(s,t) = \frac{D_o\big(\kappa_o^g - \kappa_o - \kappa_o^c\big) + D(s,t)\big(\kappa(s,t)+\kappa^c(s,t)\big)}{D(s,t)} \tag{3.3}$$

where $\kappa_o = \kappa(s,t_o)$ and $\kappa_o^c = \kappa^c(s,t_o)$. That is

$$D_o\big(\kappa^g - \kappa - \kappa^c\big) = \text{constant}. \tag{3.4}$$

However, we have determined that this special conservation does not fit our general use of the evolution equation.

3.4.2 Special Case Conservation

We remark on the use of the special condition (3.2) used to develop (3.3). Rearranging (3.3) we find that

$$D_o\big(\kappa_o - \kappa_o^g + \kappa_o^c\big) = D(s,t)\big(\kappa(s,t) - \kappa^g(s,t) + \kappa^c(s,t)\big), \tag{3.5}$$

a general form of a conservation. In [9] the special condition is satisfied with the assumption that $\dot{\kappa} = 0$, i.e., the present configuration remains static, and that $\kappa^c = 0$. These assumptions reduce (3.5) to

$$D_o\big(\kappa_o - \kappa_o^g\big) = D(s,t)\big(\kappa_o - \kappa^g(s,t)\big), \tag{3.6}$$

which is an expression for the conservation of moment in time along the arc-length.

3.4.3 The Relation of κ^c to Residual Stress

The novel function in (3.1) is the new parameter, $\kappa^c(s,t)$, which represents an induced curvature related to the change in stiffness. The source of this induction is typically related to differential growth or asymmetric residual stress in newly grown layers of material. The exact relationship between the curvature induction and the residual stress or differential growth must be prescribed, but for this dissertation we assume this prescription exists.

Residual growth stress is a significant factor in wooden plants and many times becomes a problem for the lumber industry. Lumber with high residual stress manifests itself when the tree is felled. Severe splitting develops in log ends followed by further splitting and distortion during conversion into sawn boards. Growth stresses develop in trees as they grow, which, as stated earlier, has a cumulative effect that results in counterbalancing compressive forces in the central part of the stem. This counterbalance can eventually exceed the maximum crushing strength of wood, causing numerous slip planes and compression failures; a condition generally known as "brittle heart" [18].

In a standard three-dimensional continuum mechanics based theory we can capture the residual stresses that form within a body, Hoger et al. [19]. A one-dimensional rod theory, however, does not capture the localized residual stress across the cross-section of the body. Thus, we find that κ and κ^g are incapable of accounting for the effects of residual stress. We introduce κ^c as an additional parameter to correct this deficiency.

Figure 3.6 demonstrates the subtle abstract use of κ^c. If we have two arbitrarily shaped rods, $\mathcal{L}_1$ and $\mathcal{L}_2$,(i.e., two rods with arbitrary curvature profiles) of equal length that can be fitted together to form a composite rod, we will find that residual stress exists within the composite rod when the two curvature profiles of $\mathcal{L}_1$ and $\mathcal{L}_2$ differ. The function κ^c in this example is the relative curvature between the two rods and is proportionally related to the residual stress in the composite rod.

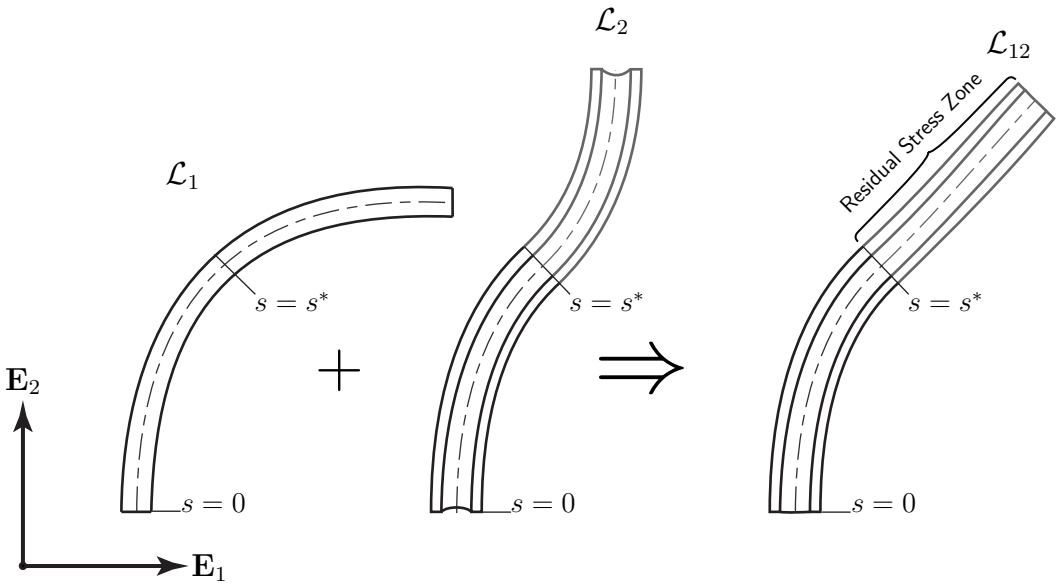

Figure 3.6: *Two rod configurations, $\mathcal{L}_1$ and $\mathcal{L}_2$, are of equal length L and have identical curvature profiles between $s = 0$ and $s = s^*$. The parameter κ^c marks the difference in curvature along the arc-length. These two rods form a composite rod configuration $\mathcal{L}_{12}$, where $\kappa^c = 0$ in $s \in [0, s^*)$ represents a zone with zero residual stress and $\kappa^c \neq 0$ in $s \in [s^*, L]$ is a residually stressed zone.*

The parameter κ^c acts like a control input for the plant. Unlike the plant's ability to change geometric and constitutive properties, the ability to control induced curvature along the arc-length of the stem over time gives the plant the most versatile control over its movement. The advantage of this evolution law with κ^c acting as a control input will be demonstrated in the subsequent sections as we show that one can setup problems by either prescribing a control input and then determine the plant's movement or prescribe the movement and determine a sufficient control input. The design of the control law for κ^c also depends on the particular tropism that is being modeled.

3.4.4 The Relevance of κ_I^g to Evolution

We also introduce the new parameter, $\kappa_I^g(s,t)$, in (3.1), which represents an induced curvature independent of the change in stiffness parameter. The source of this induction is typically not related to growth and reflects influences by non-growth related residual stress or a change in the intrinsic curvature independent of evolution, e.g., elastic hysteresis. Again, the exact relationship between the curvature induction and the residual stress must be prescribed. The exact meaning and implications of the parameter will become apparent in the following development in Section 3.5. However, κ_I^g in typically not a parameter whose change is controlled by the plant and thus our treatment focuses primarily on κ^c and (asymmetric) residual growth stress.

3.5 General Evolution Equation Features and Discrete Approximations

In order to motivate the use of the general evolution equation (3.1), we develop an evolution equation for a simple composite rod. We then adapt this problem into a discrete lateral accretion problem and derive a discrete recursive formula for the evolution of the growth configuration. The discrete evolution equation can then be shown to be an acceptable approximation of the general evolution law given the proper initial assumptions.

3.5.1 Determining the Unloaded Configuration of a Composite Rod

As illustrated in Fig. 3.7, we imagine a cantilevered rod that is straight in its initial

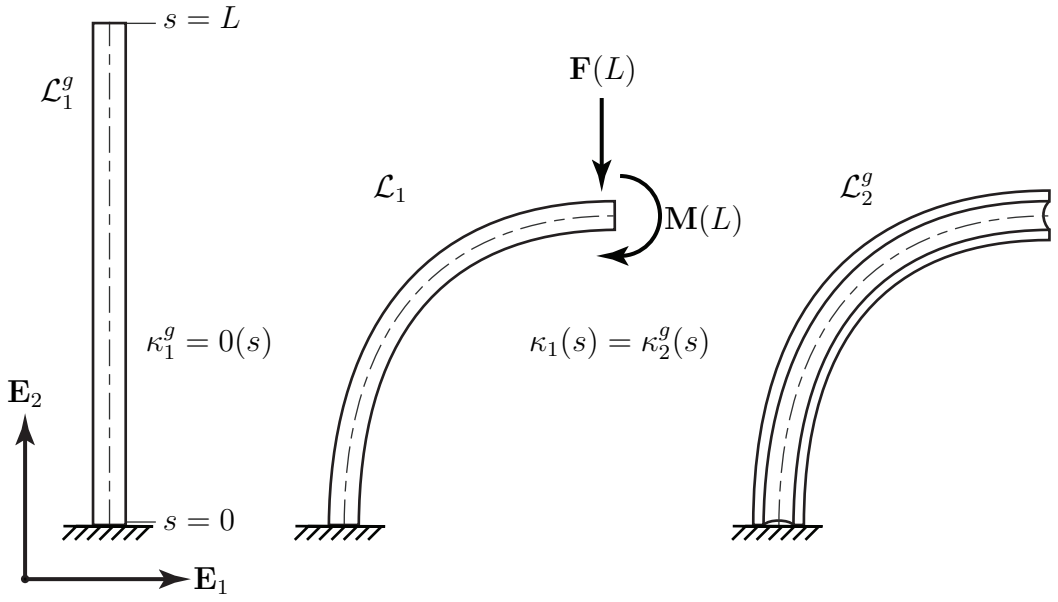

Figure 3.7: *The image on the left is the growth configuration $\mathcal{L}_1^g$ of rod 1. The middle image is the present configuration $\mathcal{L}_1$ of rod 1, and the image on the right is the growth configuration $\mathcal{L}_2^g$ of rod 2.*

(growth) configuration $\mathcal{L}_1^g$ and then bent into a deformed (present) configuration $\mathcal{L}_1$ by a force F and moment M at the tip $s = L$. We will call this rod 1 (see the left and middle drawings in Fig. 3.7). The moment in rod 1 is

$$m_1 = D_1(\kappa_1 - \kappa_1^g). \tag{3.7}$$

Without a loss of generality, now suppose that a second hollow rod (with the hollow void being equal to the space of the deformed rod 1) has an intrinsic (growth) curvature $\kappa_2^g(s)$

equal to the (present) curvature of rod 1, $\kappa_1(s)$. This rod will be called rod 2 (see the right image in Fig. 3.7) and the moment in this rod will be represented by

$$m_2 = D_2(\kappa_2 - \kappa_2^g). \tag{3.8}$$

Finally, suppose that rod 1 is fitted into the void of rod 2. We seek to determine the unloaded configuration of this composite rod.

We represent the moment in the composite rod by

$$m = D(\kappa - \kappa^g), \tag{3.9}$$

and make the following prescriptions:

$$m = m_1 + m_2, \quad D = D_1 + D_2, \quad \kappa_1 = \kappa_2 = \kappa. \tag{3.10}$$

Equation (3.9) is thus equivalent to

$$m = D_1(\kappa - \kappa_1^g) + D_2(\kappa - \kappa_2^g). \tag{3.11}$$

In (3.9), when $\kappa = \kappa^g$, then $m = 0$. If $m = 0$, then the rod combination is no longer loaded and occupies its unloaded (growth) configuration.[3] Assuming that $m = 0$ in (3.11) and solving for κ^g we find the solution for the intrinsic (growth) configuration of the composite rod:

$$\kappa^g = \frac{D_1\kappa_1^g + D_2\kappa_2^g}{D_1 + D_2}, \tag{3.12}$$

a result that can be expressed as

$$\kappa^g = \frac{D_1\kappa_1^g + (D - D_1)\kappa_2^g}{D}. \tag{3.13}$$

The combination is a weighted sum of the two intrinsic curvature profiles with the weight being the respective rod rigidity.

As mentioned above, the prescription of κ_2^g is arbitrary and that equations (3.12) and (3.13) are still valid when $\kappa_2^g \neq \kappa_1$. Additionally, D is not restricted to be constant, i.e., the rods can vary in cross-sectional area and be non-homogeneous.

3.5.2 Discrete Growth: Lateral Accretion

Below we re-imagine the problem of the composite rod in the context of a single interval of discrete lateral growth in a stem. We assume that accreted material during a growth step does not contribute sufficient weight-induced torque to significantly change the present configuration.[4] As exemplified in Fig. 3.8, the initial growth and present configuration of the stem, $\mathcal{L}^g$ and $\mathcal{L}$, respectively, are identical to rod 1 in our previous example. However,

[3] Generally, $m = 0$ does not infer that $m_1 = 0$ and $m_2 = 0$. And thus rod 1 and rod 2 hold residual stress in the unloaded composite configuration.

[4] In Section 3.4.1 we establish a simple criterion for an appropriate growth interval.

we have now added a body force induced by the acceleration field $\mathbf{g}$. We define $\mathcal{L}^g_\delta$ as the newly added layer of lateral growth represented by the image on the right in Fig. 3.8. We decompose the curvature of this growth layer $\mathcal{L}^g_\delta$ into two components,

$$\kappa^g_\delta(s) = \kappa(s) + \kappa^c(s). \tag{3.14}$$

We argue that if the accreted material does not have any *differential growth* (or does not have any asymmetric *residual growth stress*) then the newly accreted material layer has the same curvature as the present configuration, as shown by $\mathcal{L}^g_{\delta 1}$ in Fig. 3.8. If *differential growth* (or an asymmetric *residual growth stress*) is present, then the curvature of the accreted growth layer will deviate from the present configuration, as shown by $\mathcal{L}^g_{\delta 2}$ in Fig. 3.8. We define the curvature κ^c as the deviation of the growth layer curvature from the present configuration.

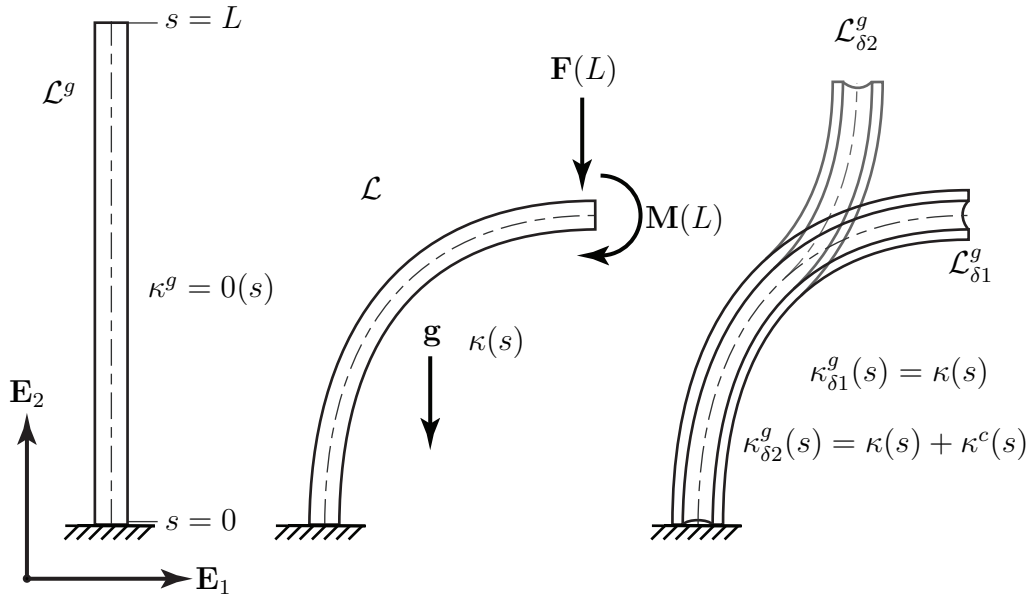

Figure 3.8: *The initial growth configuration $\mathcal{L}^g$ and present configuration of the stem $\mathcal{L}$, the left and middle image, respectively, represent a stem prior to a discrete interval of lateral growth. A body force induced by the acceleration field $\mathbf{g}$ in addition to a singular force $\mathbf{F}$ and moment $\mathbf{M}$ at the tip, $s = L$, is imposed on the present configuration $\mathcal{L}$. We define $\mathcal{L}^g_\delta$ as the newly added layer of lateral growth represented by the image on the right. When $\kappa^c(s^*) = 0$, the curvature of the present configuration $\mathcal{L}$ and the curvature of growth layer $\mathcal{L}^g_\delta$ are equal at $s = s^*$. The growth configuration $\mathcal{L}^g_{\delta 1}$ exemplifies the condition where $\kappa^c = 0$ for all $s \in [0, L]$ and $\mathcal{L}^g_{\delta 2}$ exemplifies the condition where κ^c is not necessarily zero on the interval $s \in [0, L]$.*

The new growth configuration $\mathcal{L}^g_{new}$, a composite of the lateral growth layer $\mathcal{L}^g_\delta$ and the initial growth configuration $\mathcal{L}^g$, has an associated growth configuration curvature κ^g_{new} that

is found using a similar procedure as in Section 3.5.1,

$$\kappa^g_{\text{new}} = \frac{D_o\kappa^g + D_\delta\kappa^g_\delta}{D}, \tag{3.15}$$

where D_δ is the stiffness of the lateral growth layer $\mathcal{L}^g_\delta$. Using (3.14), the curvature κ^g_{new} can also be expressed as

$$\kappa^g_{\text{new}} = \frac{D_o\kappa^g + (D - D_o)(\kappa + \kappa^c)}{D}, \tag{3.16}$$

where D_o and D are the stiffness of the stem prior to and after the accretion of material, respectively, and whose difference is

$$D - D_o = D_\delta. \tag{3.17}$$

If we continually grow discrete layers of material, (3.16) provides a recursive formula for the update of the growth configuration,

$$\kappa^g_n = \frac{D_{n-1}\kappa^g_{n-1} + (D_n - D_{n-1})(\kappa_{n-1} + \kappa^c_n)}{D_n}, \qquad n \in \mathbb{Z}^+, \tag{3.18}$$

where n is the growth step. The values of κ^c and D are prescribed and act as control input for growth related movement.

3.5.3 A Discrete Evolution Equation for κ^g Based on Constitutive Remodeling

We assume that the remodeling of a uniform rod results in an evolution equation of a form similar to (3.16) with $\kappa^c = 0$:

$$\kappa^g_{\text{new}} = \frac{D_o\kappa^g + (D - D_o)\kappa}{D}. \tag{3.19}$$

The parameter κ^c appears to have no physical relevance when an evolution occurs due to pure remodeling, and so we restrict $\kappa^c = 0$ when I is constant. We will now show that this assumption appears in the explicit solution for the special case evolution law for constitutive remodeling derived in [9].

In [9], an evolution law is established based on a static present configuration $\mathcal{L}$ for a rod that does not undergo axial or lateral growth, but whose stiffness D is changing due to constitutive remodeling. The derivation of an evolution law for this specialized case begins with the equation of the rod's moment

$$m(s,t) = D(s,t)\left(\kappa(s,t) - \kappa^g(s,t)\right). \tag{3.20}$$

Differentiating (3.20) with respect to time gives

$$\dot{m} = \dot{D}(\kappa - \kappa^g) + D(\dot{\kappa} - \dot{\kappa}^g), \tag{3.21}$$

where the superposed dot implies a partial derivative with respect to time. The static present configuration implies that the time derivative $\dot{\kappa} = 0$, while no new material that would contribute to a change in the moment arm implies that $\dot{m} = 0$. Imposing $\dot{m} = 0$ and $\dot{\kappa} = 0$ on (3.21) and solving for $\dot{\kappa}^g$ yields

$$\dot{\kappa}^g = \frac{\dot{D}}{D}(\kappa - \kappa^g). \tag{3.22}$$

This is the evolution law developed in [9].

From (3.22), we separate variables and integrate:

$$\int_{\kappa^g(s,0)}^{\kappa^g(s,t)} \frac{1}{\kappa - \kappa^g}\, d\kappa^g = \int_{D(s,0)}^{D(s,t)} \frac{1}{D}\, \mathrm{d}D. \tag{3.23}$$

That is,

$$\log\left(\frac{\kappa(s,t) - \kappa^g(s,0)}{\kappa(s,t) - \kappa^g(s,t)}\right) = \log\left(\frac{D(s,t)}{D(s,0)}\right). \tag{3.24}$$

Using the notation, $D(s,0) = D_o$ and $\kappa^g(s,0) = \kappa^g_o$, we solve for κ^g:

$$\kappa^g(s,t) = \frac{D_o(s)\kappa^g_o(s) + \big(D(s,t) - D_o(s)\big)\kappa(s,t)}{D(s,t)}. \tag{3.25}$$

This is the assumed form of the evolution equation (3.19) due to remodeling.

3.5.4 Generalized Discrete Evolution Equation

A change in curvature may occur independently of κ^c or during an instance of a configuration remodeling without accretion. We add the parameter κ^g_I to account for this situation. As a result, we find the generalized discrete evolution equation to be

$$\kappa^g_n = \frac{D_{n-1}\kappa^g_{n-1} + (D_n - D_{n-1})(\kappa_{n-1} + \kappa^c_n)}{D_n} + (\kappa^g_{In} - \kappa^g_{In-1}), \qquad n \in \mathbb{Z}^+. \tag{3.26}$$

The recursive formulation (3.26) is an adequate estimate for the continuous evolution of κ^g if the change in the present configuration between each growth step is small. More specifically, if $|\Delta(\kappa + \kappa^c)| << 1$ and $\Delta D << 1$ for an interval of time Δt, then the general evolution equation (3.1), with a slight abuse of notation, can be estimated as

$$\kappa^g = \frac{D_o\kappa^g_o + \big(\kappa + \kappa^c\big)\int_{t_0}^t \dot{D}(s,\tau)\,\mathrm{d}\tau + D\int_{t_0}^t \dot{\kappa}^g_I(s,\tau)\,\mathrm{d}\tau}{D}. \tag{3.27}$$

Invoking the fundamental theorem of calculus we find the previous equation becomes

$$\kappa^g = \frac{D_o\kappa^g_o + (D - D_o)(\kappa + \kappa^c)}{D} + (\kappa^g_I - \kappa^g_{Io}), \tag{3.28}$$

a form reminiscent of equation (3.26).

Equation (3.28) should not be confused with the special case of the continuous evolution equation (3.3), which is due to the constraint $\dot{\kappa}^g_I = \dot{\overline{\kappa + \kappa^c}}$. The estimate (3.28) is due to $|\Delta(\kappa + \kappa^c)| << 1$ and $\Delta D << 1$, which is a more likely and practical constraint. However, (3.28) and (3.3) are equivalent expressions when κ, κ^c, and κ^g_I are constants.

3.6 Analysis and Implementation of Evolution Equations and Control Laws

In this section we examine two general methods of using the evolution equation (3.1). One method is to prescribe the control input $\kappa^c(s,t)$ and stiffness evolution $D(s,t)$, and then to determine $\mathcal{L}(s,t)$, the movement of the plant configuration due to growth. The second method is to prescribe the growth movement $\mathcal{L}(s,t)$ and stiffness evolution $D(s,t)$, and then to determine $\kappa^c(s,t)$.

Restating (3.1),

$$\kappa^g(s,t) = \frac{D_o\kappa_o^g + \int_{t_0}^{t}\left[\dot{D}(s,\tau)\big(\kappa(s,\tau)+\kappa^c(s,\tau)\big)\right]\mathrm{d}\tau + \int_{t_0}^{t}\left(D(s,\tau)\dot{\kappa}_I^g(s,\tau)\right)\mathrm{d}\tau}{D(s,t)},$$

we define the integrals in (3.1) as

$$\begin{aligned} K^c &= \int_{t_0}^{t}\left[\dot{D}(s,\tau)\big(\kappa(s,\tau)+\kappa^c(s,\tau)\big)\right]\mathrm{d}\tau, \\ K_I^g &= \int_{t_0}^{t}\left(D(s,\tau)\dot{\kappa}_I^g(s,\tau)\right)\mathrm{d}\tau. \end{aligned} \tag{3.29}$$

The term $K^c(s,t)$ quantifies the net change in the intrinsic curvature κ^g due to lateral accretion, while the term $K_I^g(s,t)$ quantifies the net change in the intrinsic curvature κ^g due to influences independent of lateral accretion.

3.6.1 Determining Growth Related Movement

Recalling the general equations of motion (2.33) and that

$$\kappa(s,t) = \nu(s,t) + \kappa^g(s,t),$$

we substitute the postulated growth law (3.1) into (2.33) and develop the following set of ODEs,

$$\begin{aligned} \theta' &= \nu + \frac{D_o\kappa_o^g + K^c(s,t) + K_I^g(s,t)}{D(s,t)}, \\ \nu' &= \left(\frac{\mathcal{P}g + n_l}{D(s,t)}\right)\cos(\theta) - \frac{D'(s,t)}{D(s,t)}\nu, \\ \mathcal{P}' &= -\rho(s,t), \\ \dot{K}^c &= \dot{D}(s,t)\left(\nu(s,t) + \kappa^c(s,t) + \frac{D_o\kappa_o^g + K^c(s,t) + K_I^g(s,t)}{D(s,t)}\right), \\ \dot{K}_I^g &= D(s,\tau)\dot{\kappa}_I^g(s,\tau), \end{aligned} \tag{3.30}$$

Given valid prescriptions for $D(s,t)$ and $\rho(s,t)$, we can choose $\kappa^c(s,t)$ and $\kappa_I^g(s,t)$ as control input to induce plant movement.

Parameter	Case A	Case B	Case C
E	1.000	1.000	30×10^3 kg/cm^2
ρ^*	4.231	4.231	0.9400 g/cm^3
R_0	1.050	1.050	0.1500 cm
ΔR	0.010	0.050	0.0241 cm
L_0	1.000	1.000	5.0000 cm
ΔL	0.100	0.100	5.0000 cm
F_N	0.000	0.000	8.6200 g
N	3.000	3.000	11

Table 3.1: *The process of growth illustrated in Fig. 3.9 is simulated for three cases, where E is the modulus of elasticity, ρ^* is density, R_0 is the cylindrical radius of the primary growth segment, δR is the vertical thickness of a new added lateral growth layer, L_0 is the initial length the stem, ΔL is the incremental length of primary growth, F_N is a distributed load on the segment of primary growth, and N is the total number of incremental primary growth segments. Cases A and B are both non-dimensionalized with respect to initial length L_0.*

We now use a finite difference method to perform three simulations (Cases A, B, and C) using (3.30). For each simulation the rod undergoes primary and secondary growth as shown in Fig. 3.9. We assume that the evolution of κ^g is due to lateral accretion and no remodeling occurs. Furthermore, we assume that $\kappa^c = 0$ and $\kappa^g_I = 0$ for all time. Table 3.1 lists the parameters for each simulation. Cases A and B are both non-dimensionalized simulations with respect to initial length L_0 and are vertically cantilevered at one end ($s = 0$) and free at $s = L$. Case C is a dimensionalized simulation, which uses parameters provided by Yamamoto and Yoshida [2] to recreate a simulation for a progressively grown configuration representing a *J. chinensis* branch. The branch in Case C is horizontally cantilevered at one end ($s = 0$) and free at $s = L$.

In Fig. 3.10 we show progressive simulations for Case A of the rod growing and evolving due to lateral accretion. The evolution of the intrinsic (growth) curvature κ^g and the change in the present configuration curvature κ over time for Case A are shown in Fig. 3.11 and Fig. 3.12, respectively.

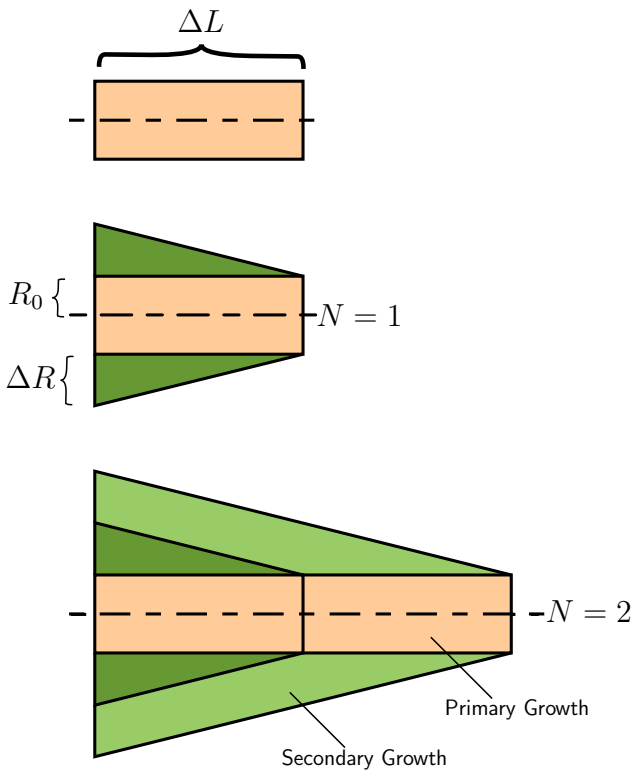

Figure 3.9: *The process of growth simulated in Cases A, B, and C for two growth steps:* $N = 1$ *and* $N = 2$*. The primary growth step length is* ΔL *with a cylindrical radius of* R_0 *about the centerline. In addition to primary growth, at each growth step a tapered layer of secondary growth is added to the rod with a thickness of* $N\Delta R$ *at the base. The rod maintains axial symmetry about the centerline.*

Likewise, in Fig. 3.13 we show the progressive simulations for Case B of the rod growing and evolving due to lateral accretion. The evolution of the intrinsic (growth) curvature κ^g and the change in curvature κ of the present configuration over time for Case B are shown in Fig. 3.14 and Fig. 3.15, respectively.

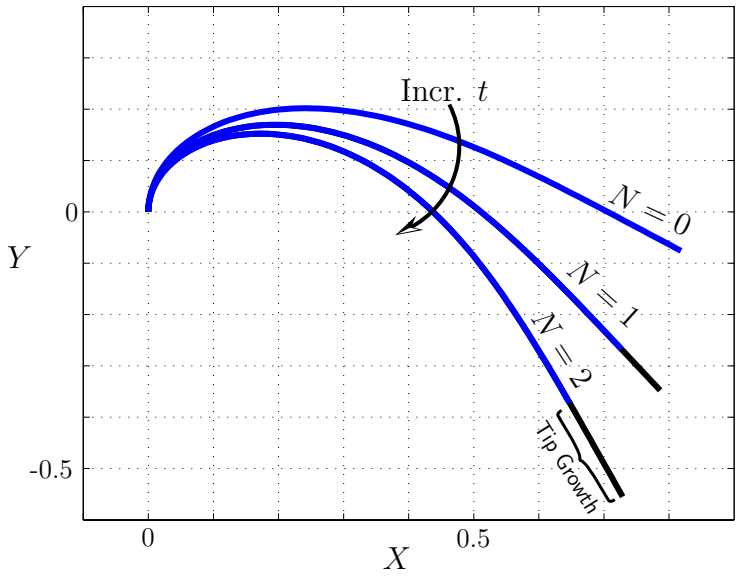

Figure 3.10: *Three successive simulations of a rod exhibiting tip growth and evolving due to a tapered lateral accretion of material are shown. The parameters for the simulation are outlined under Case A in Table 3.1.*

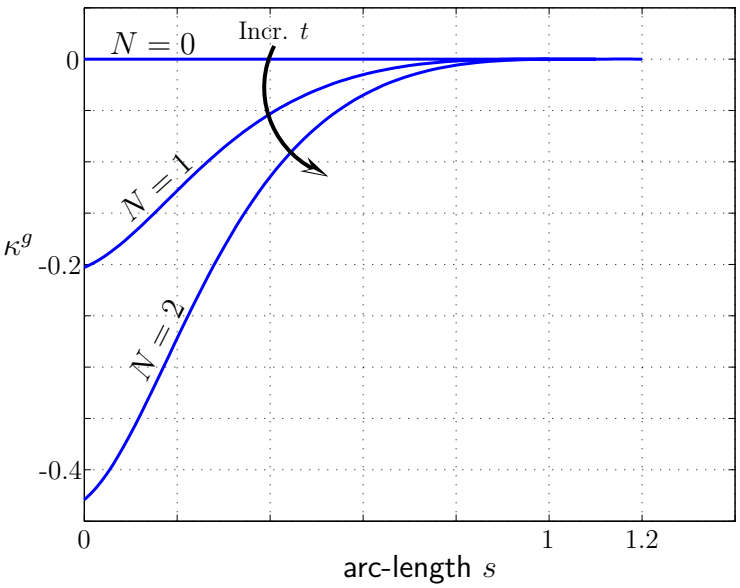

Figure 3.11: *The original intrinsic curvature profile κ^g ($N = 0$) along with two addition sequential profiles that reflect the evolution of the intrinsic curvature after two growth steps are shown above. The intrinsic curvature profiles correspond respectively to the rods shown in Fig. 3.10.*

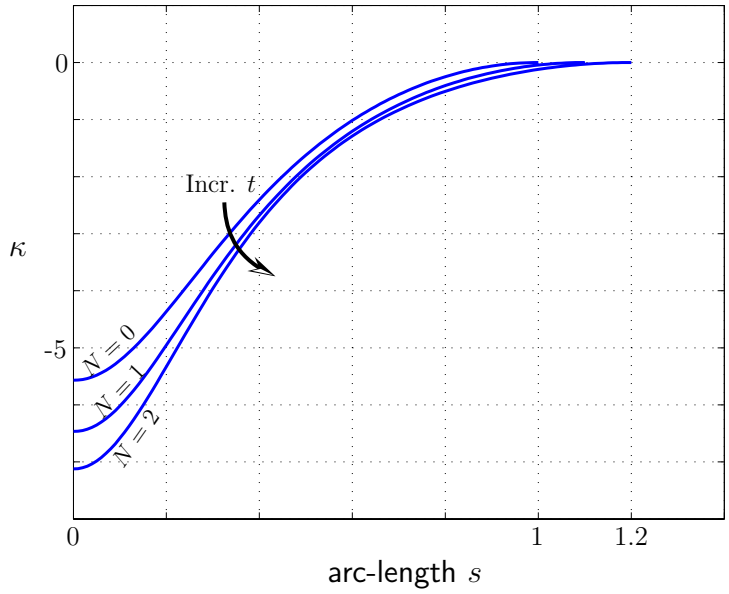

Figure 3.12: *The original present configuration curvature profile κ along with two addition sequential profiles that reflect the change in the present configuration curvature after two growth steps are shown above. The curvature profiles correlate to the rods shown in Fig. 3.10.*

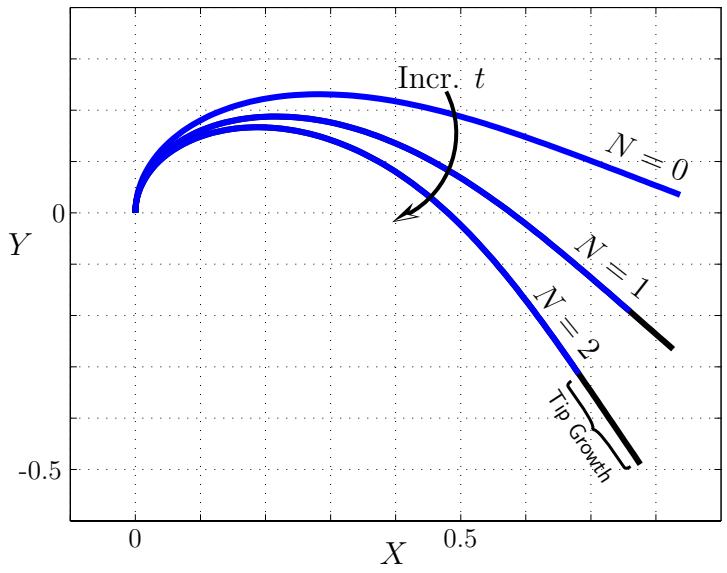

Figure 3.13: *Three successive simulations of a rod exhibiting tip growth and evolving due to a tapered lateral accretion of material are shown. The parameters for the simulation are outlined under Case B in Table 3.1.*

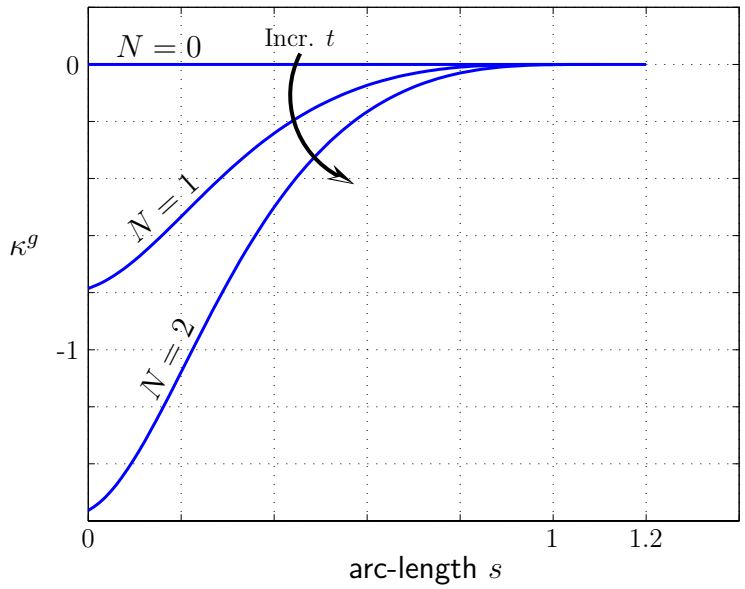

Figure 3.14: *The original present configuration curvature profile κ along with two addition sequential profiles that reflect the change in the present configuration curvature after two growth steps are shown above. The curvature profiles correlate to the rods shown in Fig. 3.13.*

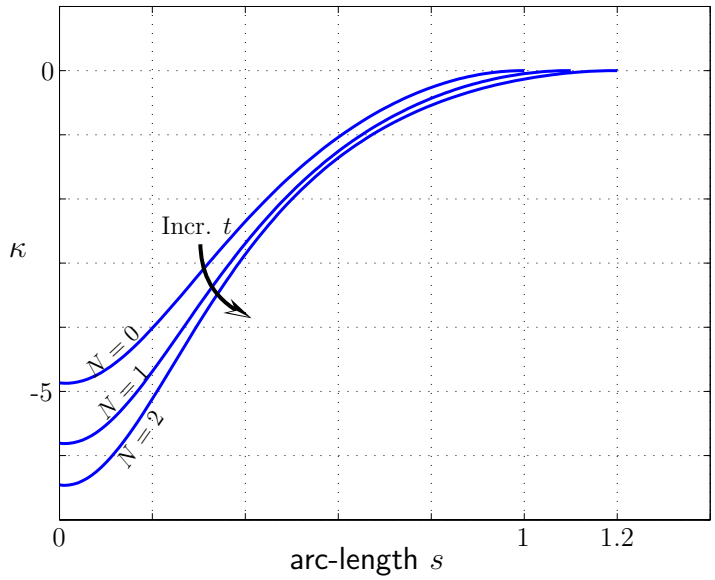

Figure 3.15: *The original present configuration curvature profile κ along with two addition sequential profiles that reflect the change in the present configuration curvature after two growth steps are shown above. The curvature profiles correlate to the rods shown in Fig. 3.13.*

The only difference in the simulation parameters in Case A and Case B is the value for ΔR. In Case A and Case B, $\Delta R = 0.01$ and $\Delta R = 0.05$, respectively. By comparing Fig. 3.16 and Fig. 3.17 we can see how a greater change in the stiffness parameter D (Case B having the greater change over time) results in the intrinsic curvature approaching the present configuration curvature more quickly. Case B also has a larger taper, which prevents the present configuration from collapsing as quickly toward the downward direction. The advantage of a taper is prevalent in many plant structures.

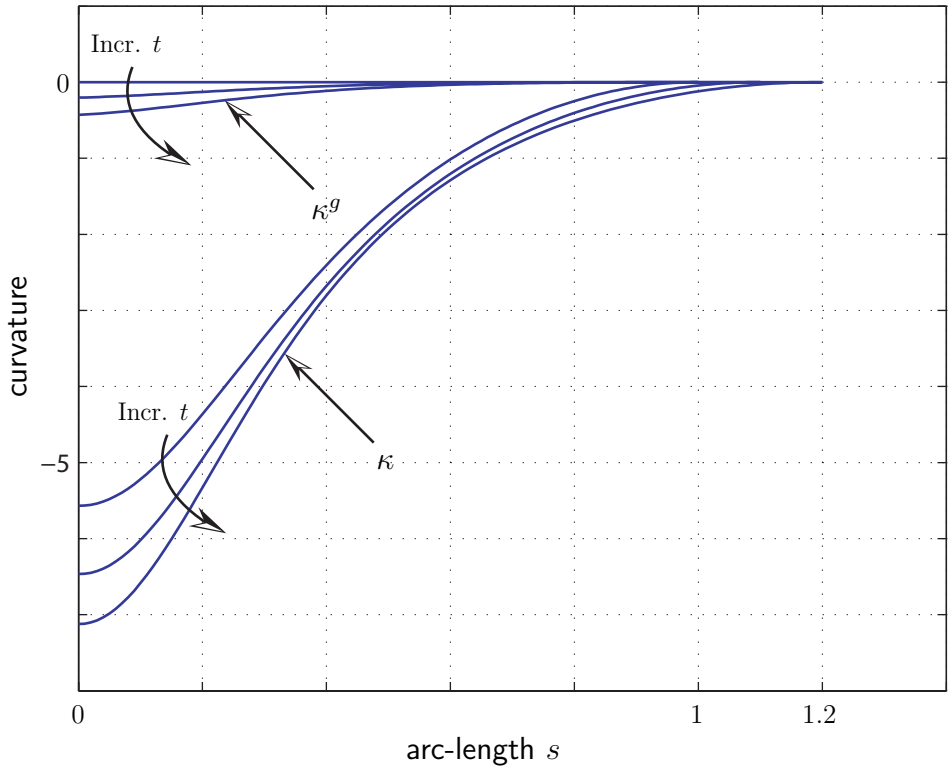

Figure 3.16: *A comparison of the intrinsic curvature profiles and present configuration curvature profiles for the rods shown in Fig. 3.10 are shown above.*

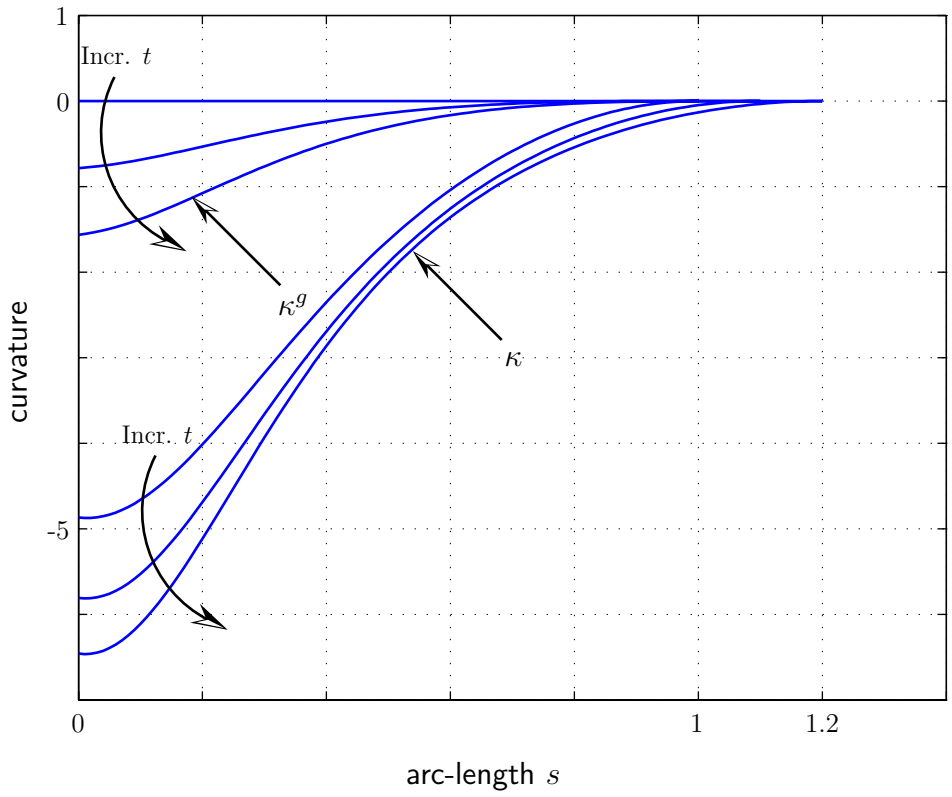

Figure 3.17: *A comparison of the intrinsic curvature profiles and present configuration curvature profiles for the rods shown in Fig. 3.13 are shown above.*

In Fig. 3.18 we compare our simulated results, Case C, with Yamamoto and Yoshida. We find that our results slightly deviate from Yamamoto and Yoshida. However, at the tip of each 5 cm primary growth interval Yamamoto and Yoshida imposed a singular vertical force that we estimated with a distributed force F_N across each 5 cm primary growth interval. Taking this into consideration, we are well within a valid range of their results. By contrast we also show in Fig. 3.18 how the final tapered configuration would look not undergone an evolution and having a constant intrinsic curvature $\kappa^g = 0$ (i.e., being a straight rod when in the growth configuration). We find that the Yamamoto and Yoshida growth methodology must make an implicit use of an evolving growth configuration.

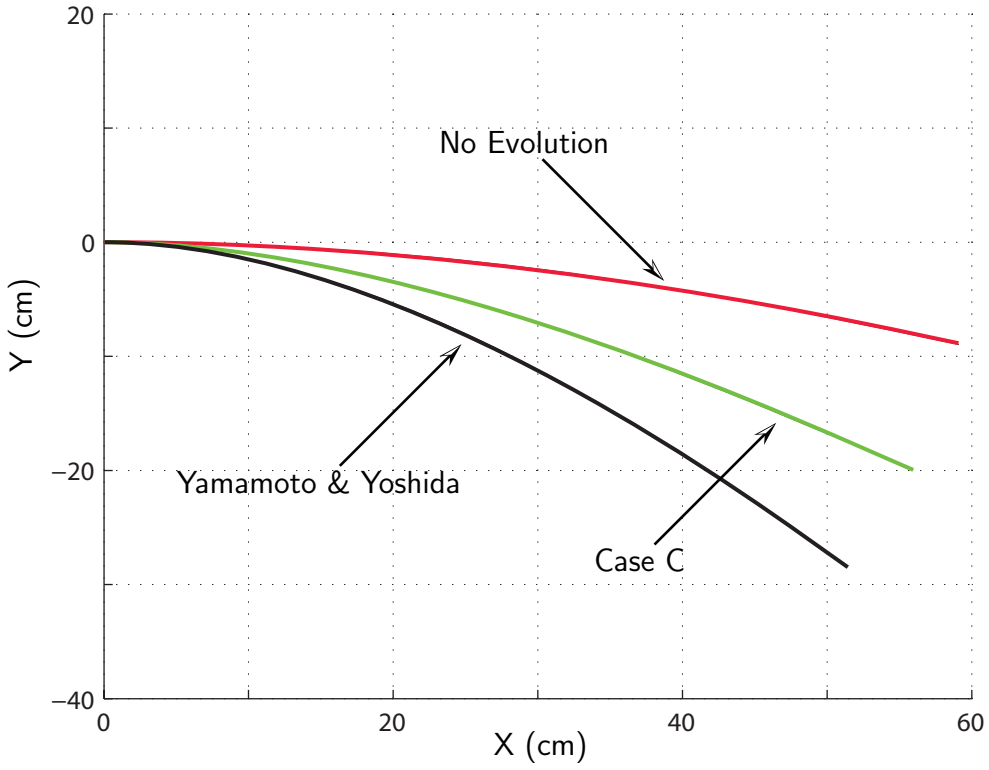

Figure 3.18: *The three curves represent simulated primary and secondary growth of three tapered rods. The results for Case C (the middle curve) were intended to reduplicate results by Yamamoto and Yoshida [2]. Yamamoto and Yoshida simulation (the bottom curve) imposed a vertical singular force every 5 centimeters, while Case C utilizes an equivalent disturbed force across the arc-length. Also shown is a tapered rod configuration (the top curve) having not undergone an evolution and having a constant intrinsic curvature* $\kappa^g = 0$.

3.6.2 Driving the Present Configuration through a Desired Path

The use and implementation of κ^c is best exemplified by deriving a control input that will induce a desired movement. To derive a control law for κ_c that will allow us to drive the initial present configuration toward a desired configuration over an interval of time we assume that $\dot{\kappa} = f$, where f is an arbitrarily prescribed movement for the branch $\big($e.g. $f = \frac{1}{\tau}(\kappa_{desired} - \kappa)\big)$. This implies that

$$\dot{\nu} = f - \dot{\kappa}^g. \tag{3.31}$$

We can invert (3.1) to solve for κ^c and arrive at

$$\kappa^c = \frac{D}{\dot{D}}(f - \dot{\nu} - \dot{\kappa}^g_I) - \nu. \tag{3.32}$$

This is the desired general control law. We generally assume that we know κ^g_I or that $\kappa^g_I = 0$. It is easy to see from (3.32) that if $\dot{D} = 0$ then the required control value κ^c

becomes indeterminate. This again reinforces the notion that κ^c is an induced sense of curvature that is strictly related to the change in stiffness.

Given f and sufficient boundary conditions we can derive $\theta(s,t)$ and $\kappa(s,t)$ which represents the desired movement of the present configuration. After establishing an initial present configuration we evolve D and any other prescribed evolution of parameters over an appropriate time interval and solve for the resulting ν via $(2.33)_{2,3}$,

$$\begin{aligned}\nu' &= \left(\frac{\mathcal{P}g + n_l}{D(s,t)}\right)\cos(\theta) - \frac{D'(s,t)}{D(s,t)}\nu,\\ \mathcal{P}' &= -\rho(s,t).\end{aligned}$$

We then determine $\dot{\nu}$, solve for κ^c using (3.32), and solve for the change in κ^g with the equation $\kappa^g = \nu - \kappa$.

The following is a simple demonstration, shown in Fig. 3.19, of a constant cross-section uniform rod that undergoes lateral accretion and exhibits tip growth over time. We desire to find $\kappa^c(s,t)$ such that $\dot{\kappa} = 0$ for all time regardless of the change in moment throughout the configuration. Again we assume that $\kappa^g_I = 0$. A static present configuration implies that $f = 0$ and

$$\kappa^c = -\frac{D}{\dot{D}}\dot{\nu} - \nu. \tag{3.33}$$

In Fig. 3.19 we see that as the tip of the branch grows, the present configuration remains constant due to growth stresses imposed by the control law. Also, we see that we can capture the phenomenon of the intrinsic curvature profile approaching the present curvature profile. Compared to Fig. 3.3, Fig. 3.19 exhibits results we are more likely to see in nature. A measure of the strain at the base of the rod $\nu(0)$, shown in Fig. 3.21, reveals that the absolute value of the strain $|\nu(0)|$ decreases with time. By contrast, the moment at the base of the rod $m(0) = D(0)\nu(0)$, shown in Fig. 3.22, reveals that the absolute value of the moment $|m(0)|$ increases with time due to the rod's tip growth.

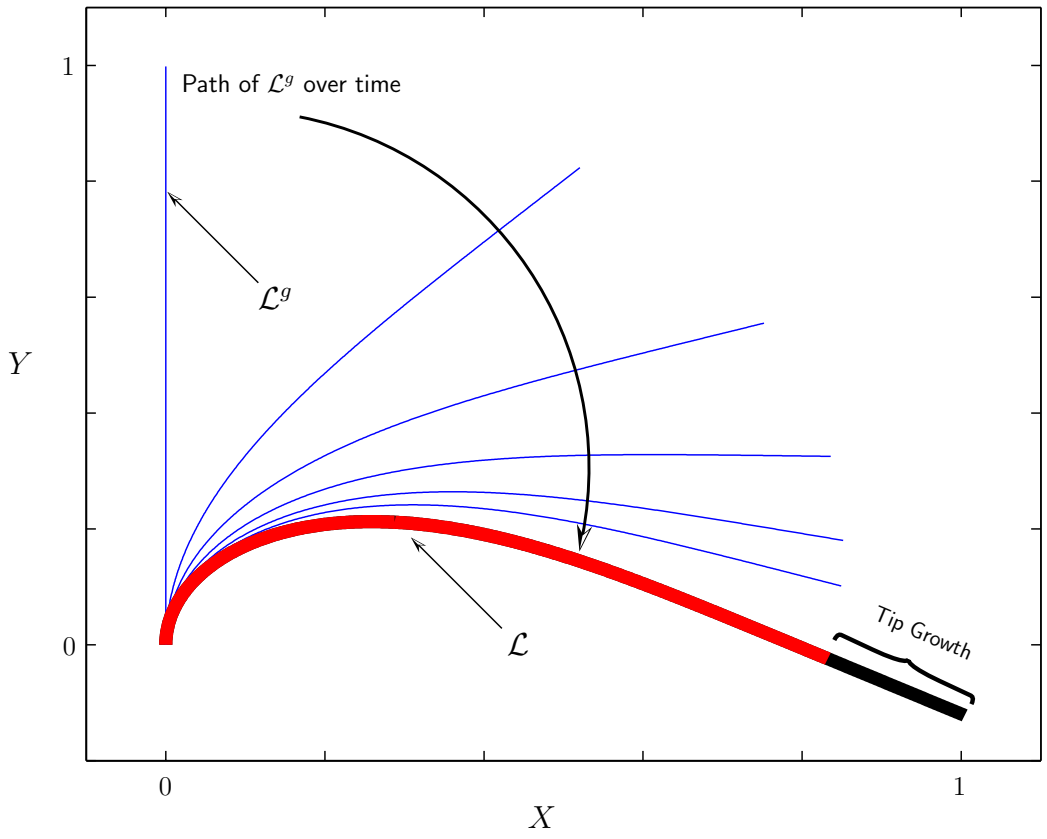

Figure 3.19: *The thick curve is a homogeneous rod of constant cross-section. The stiffness of the rod uniformly increases approximately 13 times the original value in accordance to a first order step function shown in Fig. 3.20. The time of the growth interval is divided into* 100 *equal units. The rod grows 1/5 the original length at it's tip. The thin curve represents the intrinsic configuration* $\mathcal{L}^g$ *of the original portion of the rod at distinct points in time,* $t = [0, 5, 10, 20, 40, 80, 100]$.

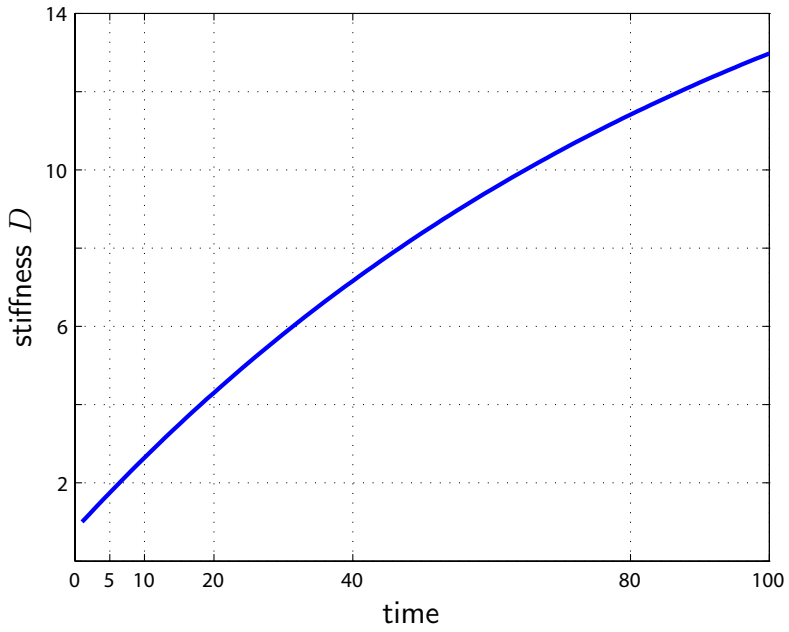

Figure 3.20: *A graph of the stiffness D of the rod in Fig. 3.19 over time.*

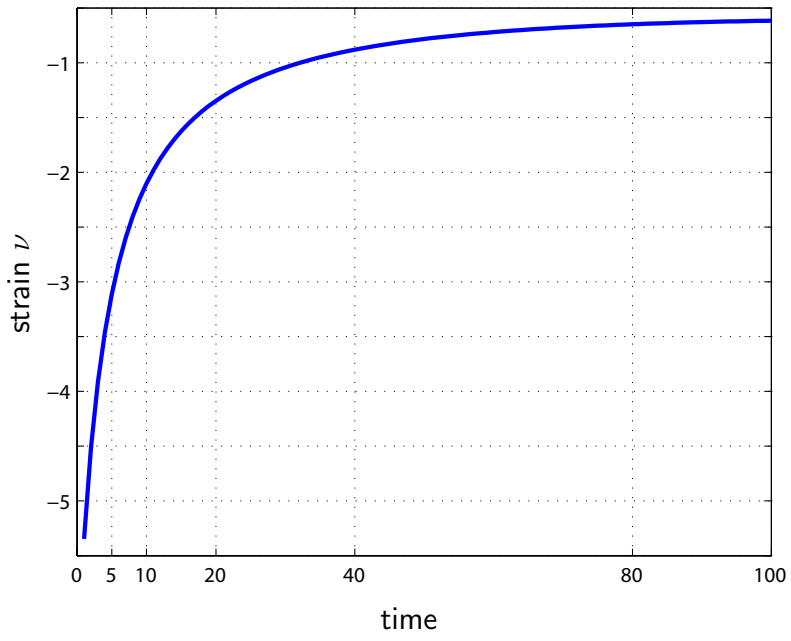

Figure 3.21: *A graph of the strain ν at the base of the rod in Fig. 3.19 over time.*

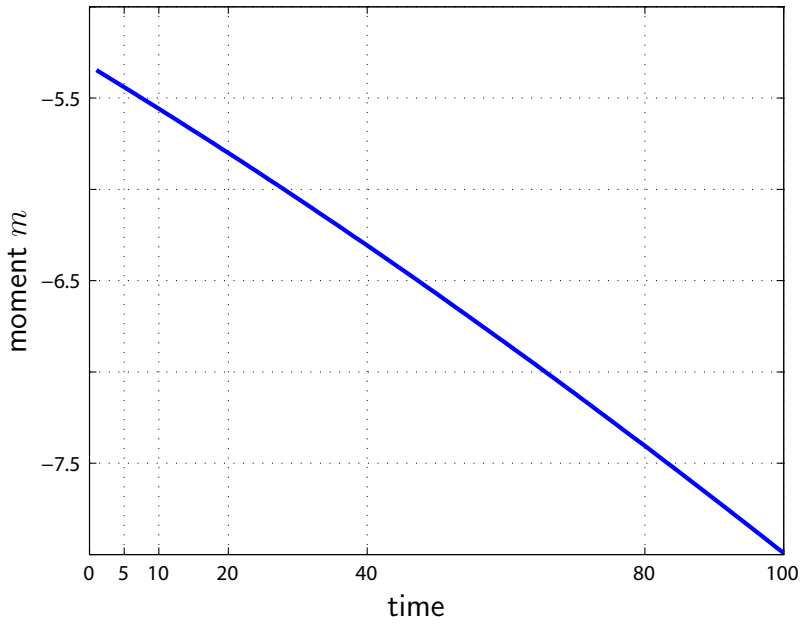

Figure 3.22: *A graph of the moment $m = D\nu$ at the base of the rod in Fig. 3.19 over time.*

3.6.3 Discussion of Tip Growth in Simulation

In various simulations, thus far, we have encountered tip growth. In the context of our evolution equations we can think of the newly developed intrinsic curvature at the tip as being apart of the initial intrinsic curvature profile κ_o^g even though it changes and grows in length over time. We assume that the initial intrinsic curvature profile κ_o^g is completely known for the entire desired final arc-length L, except that initially the values of D and ρ are zero between the arc-length values of L_o and L. Often we have prescribed no preferred angle of growth at the tip, which is indicative of a straight section of $\mathcal{L}_o^g$. However, for the simulation in Fig. 3.5 we developed the following preferred angle control law as a prescription for κ_o^g in the elongation zone at the tip,

$$\kappa^g(L_o + n\Delta L) = \frac{\theta^d - \theta_{tip}(L_o + n\Delta L)}{\Delta L}, \tag{3.34}$$

where L_o is the original total length of the branch, n is the current time growth step number, ΔL is the step length, and θ^d is the preferred angle of growth. Equation (3.34) gives us a curve initial intrinsic curvature. If evolution is present then once the curvature is prescribed at the tip it can then evolve away from this value according to the evolution equations.

3.6.4 Decomposition of κ^g

From (3.1) we can decompose κ^g into the relevant contributions of the change in κ^g over time. Adding $\left(D\kappa_o^g - D\kappa_o^g\right)/D$ to the left side of (3.1) and rearranging terms we can

arrive at

$$\kappa^g = \kappa^g_o + K^g_{SS} + K^g_{AS} + \frac{K^g_I}{D}, \tag{3.35}$$

where

$$\begin{aligned} K^g_{SS} &= \frac{\int_{t_0}^{t} \left[\dot{D}(s,\tau)\big(\kappa(s,\tau) - \kappa^g_o(s)\big)\right] \mathrm{d}\tau}{D}, \\ K^g_{AS} &= \frac{\int_{t_0}^{t} \left[\dot{D}(s,\tau)\kappa^c(s,\tau)\right] \mathrm{d}\tau}{D}. \end{aligned} \tag{3.36}$$

The integral K^g_{SS} represents the change in κ^g due of the development of symmetric residual stresses in the growth layer. The integral K^g_{AS} represents the change in κ^g due to the development of asymmetric residual stresses in the growth layer. Again, the asymmetric residual stress is the means by which heavy branches remain upright.

3.7 Comments on Decreasing Stiffness

In the previous sections we have developed evolution equations for the intrinsic curvature κ^g based on the time-related increase of the stiffness parameter D, either by an increase of the modulus of elasticity E or by an increase of the cross-sectional moment of inertia I. In the following we discuss the issue of decreasing stiffness by first considering a few physical examples. However, a conclusive model for the change in the growth and present configurations due to a drop in stiffness D is left for future work.

A straight piece of dry spaghetti provides an example of a softening rod. After allowing a strand of spaghetti to briefly soften in boiling water, we allow the strand to hang in an inverted configuration (i.e., holding it upright with your fingers at the base). We find that the strand's, formally straight, growth configuration will approach the present hanging configuration as it dries (and the modulus of elasticity E increases) as predicted by (3.25). In this new present configuration, we again allow the stiffness to decrease (possibly by the introduction of stream). According to the evolution equation for remodeling (3.25) we would find a very non-physical result. The growth configuration would return to its initial straight configuration. If we were to continue to decrease the stiffness, the growth configuration would continue to diverge from the present configuration. In reality, we find that the growth configuration remains constant and that the present configurations changes by hanging lower to the ground due to the configuration's inability to support it's own self-weight.

We find that we can generally assume that an evolution of κ^g influenced by the present configuration does not occur when stiffness decreases. Instead, the intrinsic (growth) curvature κ^g of a uniform rod with no residual stress will be held constant as stiffness decreases due to either $\dot{E} < 0$ or $\dot{I} < 0$.

The situation is different for a rod with residual stress. It is possible for the stiffness to change in a way that allows a shift in the balance of residual stress that changes the growth configuration. How to properly model this situation will be one of the subjects of our future work.

Chapter 4

Preferred Configurations

When we model plants, we assume that the simulated configurations that represent a *natural* configuration are stable configurations. In other words, the determination of stability of our simulated configurations becomes important in determining whether the configurations accurately portray physical configurations. In the following sections, we define stability and then give a brief overview of classical and modern treatments of rod stability with respect to a buckling column. We then develop a numerical analysis technique called the S-curve, which allows us to isolate a *preferred* set of stable rod configurations for a single rod and identify a phenomenon that will be called *jumping points*. The preferred set of configurations does not always encompass all of the stable configurations in a family of solutions for a particular rod. However, we contend that the preferred set represents a set of physically realizable solutions. In the next chapter we extended the use of isolating preferred configurations to configurations with multiple branches. Our discussion and use of the S-curve is based on the equations of motion (2.33). Although, much of our work is exemplified using the reduced order equations of motion (2.38),

$$\begin{aligned}\frac{\partial\theta}{\partial s} &= \nu + \kappa^g,\\ \frac{\partial\nu}{\partial s} &= \frac{1}{D}\big(\rho g(L-s) + n_l\big)\cos(\theta).\end{aligned}$$

4.1 Rod Stability

Stability requires that the configuration of a rod, under a small perturbation, return to its original configuration. More formally, we define stability for a rod configuration by the following definition:

Definition (*Asymptotic Stability*) The configuration corresponding to the static position vector $\mathbf{r}_o(s)$ $\forall s \in [0, L]$ is said to be stable if, given $\epsilon > 0$, there exists a $\delta = \delta(\epsilon) > 0$ such that, for any non-static solution, $\mathbf{r}(s,t)$, satisfying $\|\mathbf{r}(s,t) - \mathbf{r}_o(s)\|_I < \delta$ (where $\|\cdot\|_I$ is a norm on $\mathbb{R}^2$), then $\|\mathbf{r}(s,t) - \mathbf{r}_o(s)\|_I < \epsilon$ for $t > t_o$, $t_o \in \mathbb{R}$, and there exists a constant $b > 0$ such that, if $\|\mathbf{r}(s,t) - \mathbf{r}_o(s)\|_I < b$, then $\lim_{t\to 0} \|\mathbf{r}(s,t) - \mathbf{r}_o(s)\|_I = 0$.[1]

[1]The solution of $\mathbf{r}(s,t)$ satisfies the non-static equations of motion for an elastica.

For an arbitrary vector function $\mathbf{v}(s)$ on the configuration we define the norm $\|\mathbf{v}(s)\|_I$ as the following:

$$\|\mathbf{v}(s)\|_I = \int_0^L \mathbf{v}(s^*) \cdot \mathbf{v}(s^*) \mathrm{d}s^*. \tag{4.1}$$

In order for any rod configuration to fulfil the requirement of asymptotic stability we assume a sufficient amount of internal friction.

4.2 The Buckling Column and Stability

The classic problem of the tallest prismatic, i.e., constant cross-section, column that does not buckle under its own self-weight was solved by Euler [20, 21]. Euler's solution provides a boundary for rod stability for a simplified configuration. This boundary is marked by the threshold of the column that buckles versus the column that does not buckle under its own self-weight. Since then, others such as Keller and Niordson [22, 23], have revised the conditions of the classical problem to investigate the tallest tapered cross-section column given a constant volume. The starting point of these investigations were all based on the Bernoulli-Euler beam theory, where curvature is proportional to bending moment. Keller and Niordson reformulated the classical Euler problem into an eigenvalue problem, where the least eigenvalue was maximized over a class of shapes. In [24] the critical height of an unloaded column under its own self-weight is said to be the fourth root of the least eigenvalue of a certain Sturm-Liouville operator. Most recently, the method used by Keller and Niordson was revisited by Cox and McCarthy [24] and Neu and Farjoun [25], who question certain assumptions and conclusive results made by Keller and Niordson [22, 23].

The aforementioned work shows that the analytical determination of rod stability for simple configurations under specialized constraints is a non-trivial body of work. In the sequel, we introduce numerical methods to aid in stability analysis for reasonably more complex configurations than those previously mentioned. However, in order to make a transparent relation of our analysis method to the previously mentioned analytical treatments, we introduce a problem similar to that of Euler's prismatic column.

4.2.1 Euler's Column and a Cantilevered Rod

Using (2.38), we setup a boundary value problem for a single cantilevered rod under the influence of gravity that is free from contact forces and moments at the tip $s = L$ while being constrained at the base $s = 0$ by a force and moment. We prescribe zero intrinsic curvature, $\kappa^g = 0$, over the entire length of the rod.

Given the above prescriptions, $n_l(L) = 0$ and $\kappa^g(s) = 0,\ \forall s \in [0, L]$, (2.38) becomes

$$\begin{aligned} \frac{\partial \theta}{\partial s} &= \kappa, \\ \frac{\partial \kappa}{\partial s} &= \frac{\rho g}{D}(L - s)\cos(\theta). \end{aligned} \tag{4.2}$$

Clearly, (4.2) can be non-dimensionalized by the length of the rod L in the following way:

$$\begin{aligned} \frac{\partial \theta}{\partial \hat{s}} &= \hat{\kappa}, \\ \frac{\partial \hat{\kappa}}{\partial \hat{s}} &= \alpha\big(1-\hat{s}\big)\cos(\theta), \end{aligned} \tag{4.3}$$

where

$$\alpha = \frac{\rho g}{D} L^3, \quad \hat{\kappa} = \kappa L, \quad \hat{s} = \frac{s}{L}. \tag{4.4}$$

The parameter α is inversely proportional to stiffness and can be thought of as a non-dimensional compliance (or inverse stiffness) parameter.

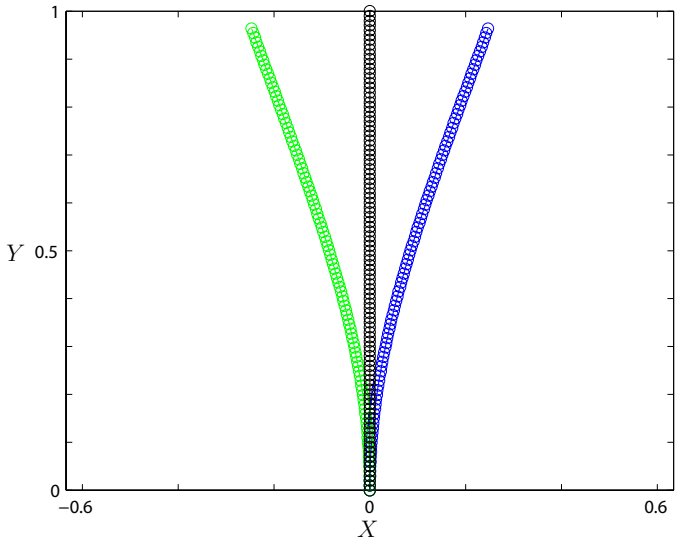

Figure 4.1: *When $\alpha = 8$ the inverted rod, the middle configuration of unit length, is unstable and will fall to one of two stable configurations, the left or right configuration, if slightly perturbed. Thus, a BVP with boundary conditions of $\hat{\kappa}(1) = 0$ and $\theta(0) = 90^\circ$ will have three solutions: two stable and one unstable.*

Euler initially found that a homogeneous constant cross-section column under its own self-weight has a critical height of

$$L_c = \left(\frac{9D}{4\rho g} j_{-1/3}^2\right)^{1/3}, \tag{4.5}$$

where $j_{-1/3} \approx 1.8663$ is the least positive root of the Bessel function of order $-1/3$. Thus, when the cantilevered rod is in an inverted configuration and represents a column under its own self-weight at a critical height L_c, the critical non-dimensional compliance parameter α_c is

$$\alpha_c = \frac{9}{4} j_{-1/3}^2 \approx 7.84\,. \tag{4.6}$$

The column is unstable for any value of $\alpha > \alpha_c$.

In Fig. 4.1, three simulated rods represent the configurations that arise for an intrinsically straight rod of unit length with $\alpha = 8$ and boundary conditions of $\hat{\kappa}(1) = 0$ and $\theta(0) = 90°$. There are two stable configurations and one unstable configuration (represented by the column).

The first boundary condition is a prescribed moment at the tip, which in the case of the simulations shown in Fig. 4.1 is the constraint of having zero moment at the tip. From (2.24), zero moment implies zero strain (i.e., $\hat{\kappa}(1) = 0$) since D is always non-zero. A problem arises in choosing the second boundary condition as it is unclear from our choice whether the rod is stable or unstable.

Generating configurations with a shooting method demonstrates that for some boundary conditions there are multiple solutions that are a combination of stable and unstable configurations. Insight into rod stability versus our choice of boundary conditions is gained through a numerical comparison of closely related configurations generated from a series of IVPs.

4.3 The S-curve

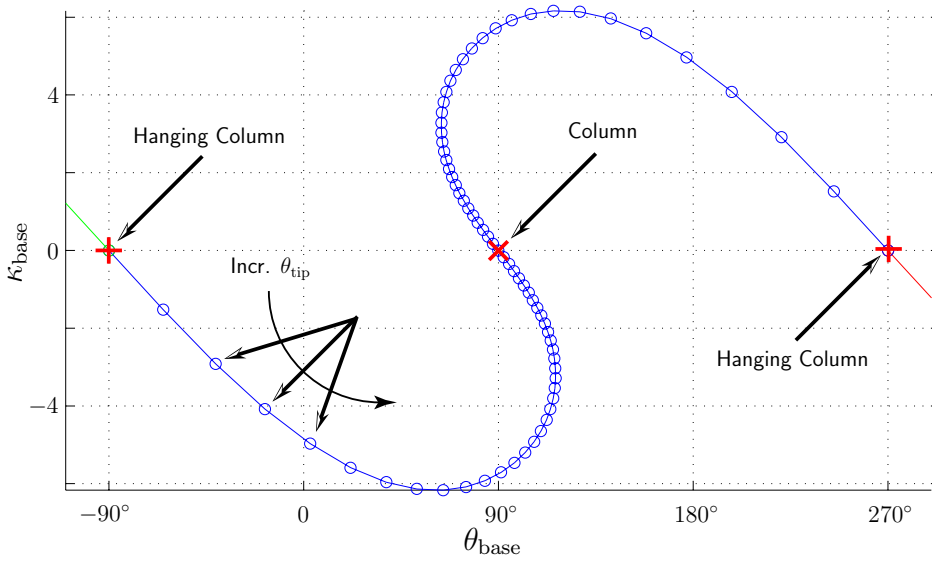

Figure 4.2: *S-curve: The value of θ_{tip} is varied at 5° intervals between the set $[-90°, 270°]$ with $\alpha = 15$. The intervals of θ_{tip} are represented by circles on the curve. Points on the continuous S-curve represents all the possible configurations for a single free-end rod that has unstable configurations. The X in the middle represents the inverted rod, which is unstable for this system. The crosses represent the same straight hanging rod configuration. Since θ_{tip} is prescribed at equal intervals it can be observed that there is a non-uniform stretch to the curve.*

Again, working with the simplified non-dimensionalized form of the equation of motion (4.3), we choose to integrate backwards from the rod tip, $\hat{s} = 1$, to the base, $\hat{s} = 0$. For simplicity we let

$$\begin{aligned} \kappa_{\text{tip}} &= \hat{\kappa}(1), \\ \theta_{\text{tip}} &= \theta(1), \\ \kappa_{\text{base}} &= \hat{\kappa}(0), \\ \theta_{\text{base}} &= \theta(0). \end{aligned} \tag{4.7}$$

We are given the initial value condition $\kappa_{\text{tip}} = 0$ and choose a value of θ_{tip} from a range of values between $[0°, 360°]$. Proceeding to integrate backwards, we find that each value of θ_{tip} corresponds to a unique rod configuration. From a series of IVP configurations generated in a way just described, we create the S-curve.

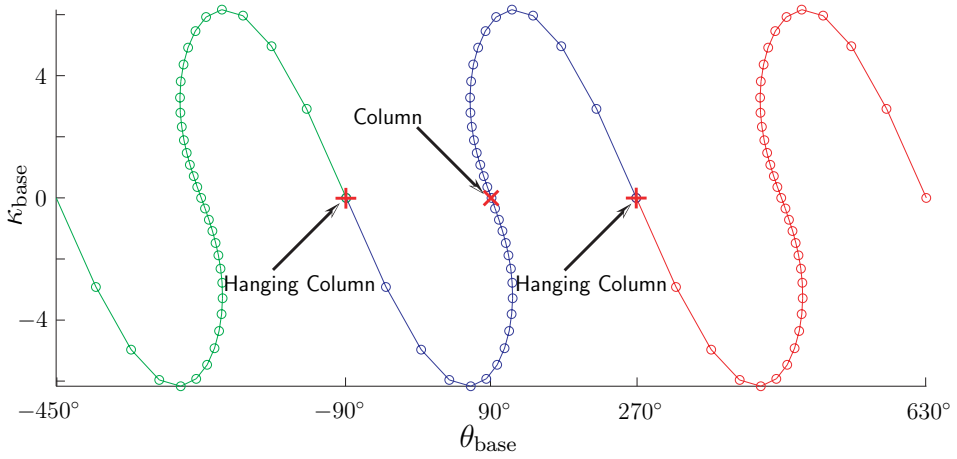

Figure 4.3: *S-curve: The same curve in Fig. 4.2 is shown with the range of θ_{base} expanded to show the periodic nature of the S-curve within* 360° *interval of θ_{base}. The value of θ_{tip} is varied at* 10° *intervals between the set* $[-450°, 630°]$ *with* $\alpha = 15$.

The S-curve takes advantage of our ability to numerically store the strain and angle states at the tip and base of a rod. The S-curve, exemplified in Fig. 4.2, is a curve parameterized by θ_{tip} with the X-axis and Y-axis representing the base angle θ_{base} and the non-dimensional strain[2] at the base κ_{base}, respectively. The curve has non-uniform stretch since equal intervals of θ_{tip} tend not to produce equal arc-length intervals along the curve. We observe the stretch in Fig. 4.2 and Fig. 4.3 by the relative change in arc-length distance between circles on the S-curve. Again, the circles represent equal intervals of θ_{tip}. In Fig. 4.3 we observe that the S-curve is generally periodic with respect to 360° intervals of θ_{base}. Additionally, each value of the non-dimensionalized compliance α results in a unique continuous S-curve, where each point on the S-curve in a 360° interval of θ_{base} corresponds to a unique rod configuration.

[2]In this case, the non-dimensional strain $\hat{\nu}$ equals curvature $\hat{\kappa}$ since $\hat{\kappa^g} = 0$.

4.3.1 S-curve's Relation to the Tallest Column

Recall that a low value of α represents a stiff, light or short rod, while a high value of α represents a very flexible, heavy or long rod. As α is varied to produce various S-curves there is a bifurcation point, $\alpha = \alpha_b$, where S-curves corresponding to values of $\alpha < \alpha_b$ can be represented by a graph, i.e., all the configurations have a unique correspondence to a value of θ_{base}.

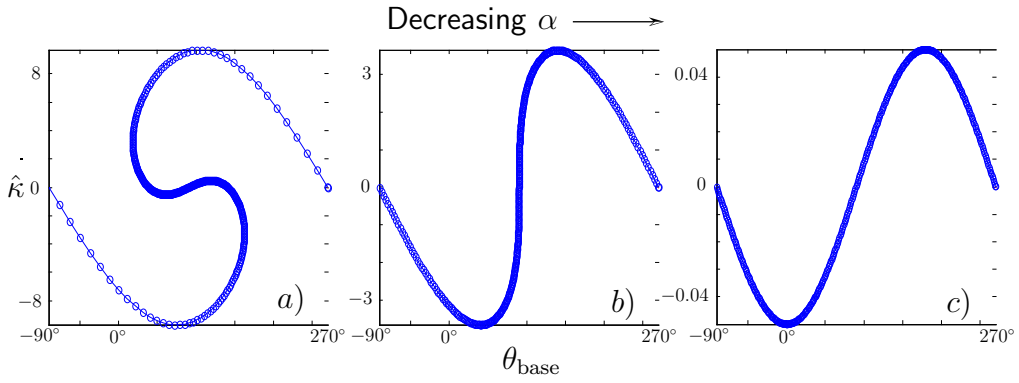

Figure 4.4: *For a free end rod without intrinsic curvature we find that when α is less than 7.84 the curve can be represented by a graph. Also, notice that as α decreases the degree of non-uniform stretch in the curve also decreases. As the value of α approaches the representation of a rigid straight rod the curve approaches the analytical solution of $D\kappa \approx -\frac{m_r g L}{2}\cos(\theta)$. a) The curve with $\alpha = 30$ contains stable and unstable configuration. b) The graph with $\alpha = 7.845$ shows the bifurcation points between the family of α-configurations with unstable solutions and without unstable solutions. The inverted rod (or column) is critically stable. c) The graph with $\alpha << 1$ contains configurations which are all stable configurations. The graph is a negative cosine with respect to the origin.*

For the case of a straight cantilever (i.e., a rod without intrinsic curvature and no force and no moment at the tip) $\alpha_b = 7.84$. This particular bifurcation point is the same as the critical buckling point Euler calculated for a column under its own self-weight. As we vary α, as exemplified in Fig. 4.4, we find that as the compliance parameter approaches a value of $\alpha << 1$, the functional relationship between κ_{base} and θ_{base} approaches the analytical solution for a rigid straight rod,

$$D\kappa_{\text{base}} \approx -\frac{m_r g L}{2}\cos(\theta_{\text{base}}), \tag{4.8}$$

where $m_r = \rho L$ is the total mass of the rod.

4.3.2 Using the S-curve for Stability Analysis

The parameter α is insufficient to determine when unstable configurations appear for rod configurations more complex than a homogeneous constant cross-section cantilever.

Additionally, we desire a means of distinguishing stable and unstable solutions. Thus, the S-curve is an insightful tool for stability analysis. Furthermore, there is an additional phenomenon where certain rod configurations will act similar to critically stable rods, but will jump to more stable configurations if perturbed in a particular way. These rod configurations exist as distinct points on the S-curve and are call *jumping points*.

Finding a preferred set of stable configurations and jumping points with the S-curve is achieved by adding an additional axis to the curve. As we mentioned previously, each point on the S-curve represents a rod configuration. Each configuration has an associated potential energy.

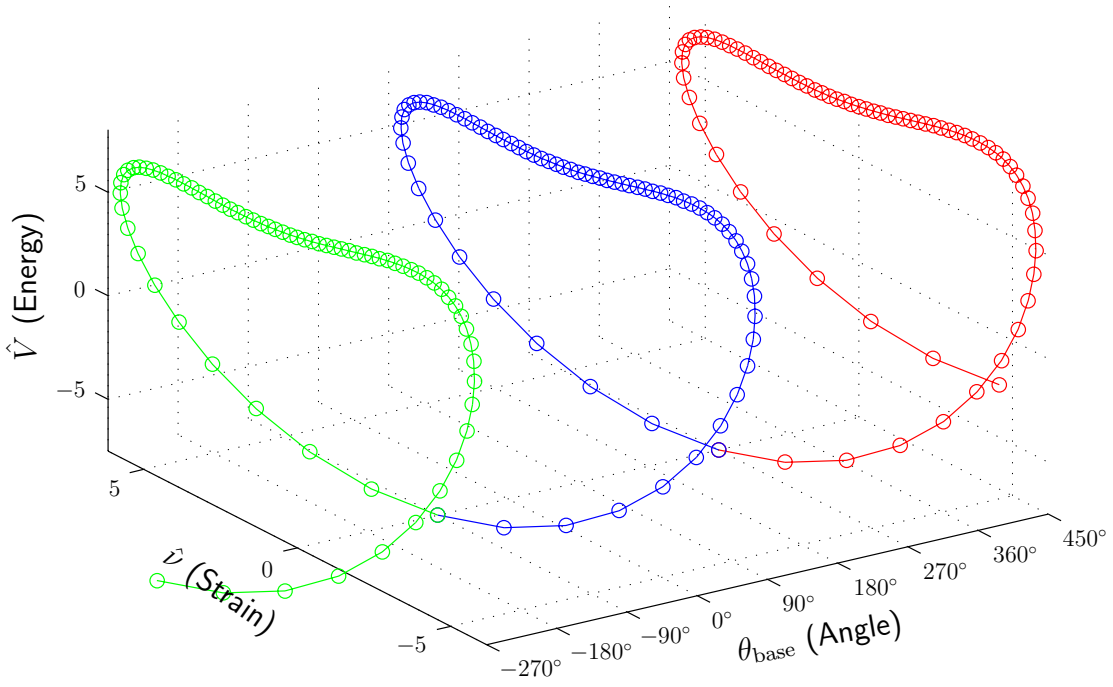

Figure 4.5: *The three dimensional curve represents a homogeneous constant cross-section cantilever with* $\alpha = 15$. *The projection of the curve onto the strain-angle plane is the S-curve shown in Fig. 4.3. The projection of the curve onto the strain-angle plane and the energy-angle plane is shown in Fig. 4.6.*

Using the energy functional used to re-derive the equations of motion (2.33) in Appendix A, the total potential energy of a particular configuration is represented by[3]

$$V = \int_0^L \left[\frac{1}{2} D(s)(\theta' - \kappa^g(s))^2 + \mathcal{P}(s) g \sin(\theta) + n_l \sin(\theta) \right] \mathrm{d}s, \tag{4.9}$$

[3]See Appendix A for an explanation of the grouped terms in (4.9).

where the energy V can also be non-dimensionalized with respect to the rod length L, which is denoted as $\hat{V}$.

A plot with the third axis representing the energy given by (4.9) along with the S-curve is shown in Fig. 4.5. A view of the plot projected onto the strain-angle plane is shown at the top of Fig. 4.6. In this view we have our typical S-curve. A view of the plot projected onto the energy-angle plane is shown at the bottom of Fig. 4.6.

We make the following conjectures with respect to the three-dimensional curve in order to make use of the S-curve:

- In the strain-angle plane[4], intervals of θ_{base} where the value of θ_{base} corresponds to a unique configuration, represents an interval of stable configurations.

- In the energy-angle plane, the point on the projected curve that corresponds to the lowest energy is a stable configuration.

- Starting at a point on the curve that represents a stable configuration, as we move along the curve with respect to an increasing or decreasing curve parameter θ_{tip} we pass through points that represent additional stable configurations until we reach a jumping point.

- A jumping point in the strain-angle plane is identified by a point that borders an interval of stable configurations. At that point on the S-curve the following holds true
$$\frac{\partial \hat{\nu}}{\partial \theta_{\text{base}}} = \infty. \tag{4.10}$$

- At a jumping point, if the configuration is perturbed in a direction away from neighboring stable configurations on the curve then the configuration will jump to a point on the curve in the energy-angle plane that corresponds to lowest energy for a value of θ_{base} equal the value of θ_{base} at the jumping point.

Using the previous conjectures we can isolate a set of stable configurations. The thick curves in Figure 4.6 represent the stable configurations, while the vertical arrows indicate the location and direction of jumping points.

This method of determining a stability set can be extended to reasonably more complex rod configurations. In Fig. 4.7 the S-curve is generated for a rod with intrinsic curvature $\kappa^g \neq 0$, varying density ρ, and varying stiffness D along the length of the rod. The rod is anchored at the base, but has a vertical singular force $\mathbf{F}$ imposed at the tip. Again, the preferred stable configurations are represented by points on the thick curve.

[4]For brevity, an explicit reference to the *strain-angle* plane or *energy-angle* plane refers to the projection of the three-dimensional curve onto that plane.

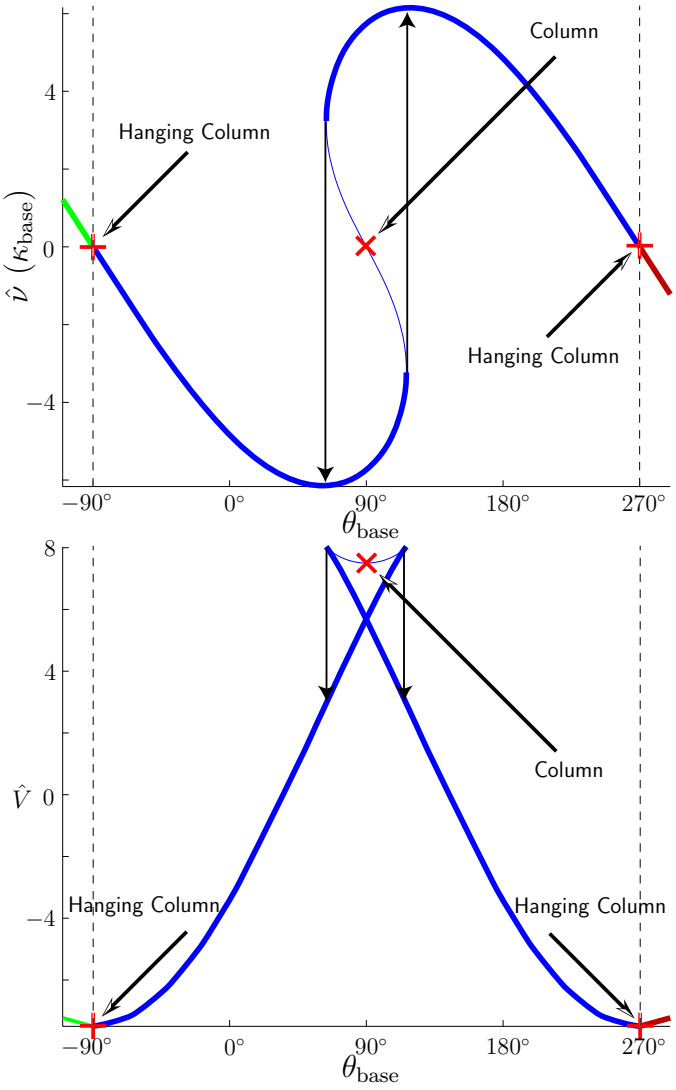

Figure 4.6: *The value of θ_{tip} is varied at an interval of $[-90°, 270°]$ with $\alpha = 15$. This S-curve represents all the possible configurations for a single free-end rod with no intrinsic curvature. The X in the middle represents the inverted rod, which is unstable for this system. The crosses represent the same straight hanging branch configuration. The stable configuration are represented by points on the thick curve, while the unstable configurations are represented by points on the thin curve. The vertical arrows represent the location and direction of jumping point with the actual jumping point at the end of the arrow and the new stable configuration at the arrowhead.*

For particular situations, the previous conjectures allow us to separate the stable and unstable solutions. However, it is possible to not completely isolate the entire set of stable solutions in the S-curve. We have found that the stable solutions we cannot isolate are typically not attained by physical plant configurations and given a sufficiently large perturbation the rod configuration will settle into the set of stable solutions we have isolated

with our S-curve analysis. In the next chapter, the isolated stable configuration set is used in the process of generating solutions for stable branched configurations.

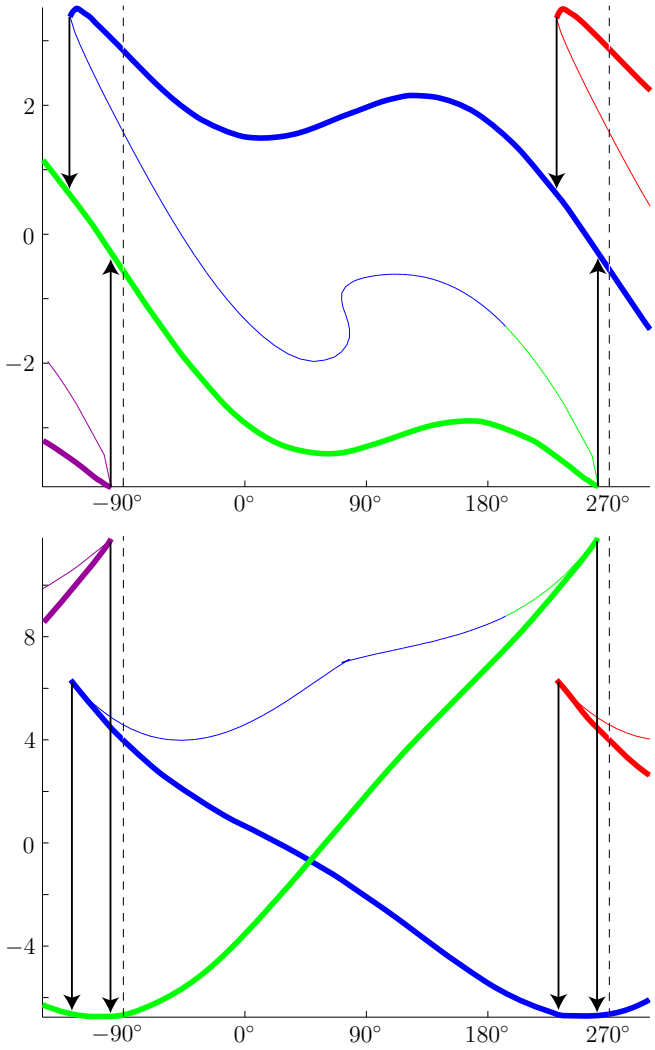

Figure 4.7: *This S-curve represents a rod with intrinsic curvature $\kappa^g \neq 0$, varying (sinusoidal) density ρ, and varying (sinusoidal) stiffness D along the length of the rod. The rod is anchored at the base, but has a vertical singular force $\mathbf{F}$ imposed at the tip. The stable configuration are represented by points on the thick curve, while the unstable configurations are represented by points on the thin curve. The vertical arrows represent the location and direction of jumping point with the actual jumping point at the end of the arrow and the new stable configuration at the arrowhead. The dashed vertical lines section out a* 360° *interval that the S-curve repeats every* 360° *of θ_{base}.*

4.3.3 Physical Example of a Simplified S-curve

For the particular rod used to generate the curves in Fig. 4.2 and Fig. 4.3, we recall that the rod has zero intrinsic curvature. The observed symmetry is peculiar to the case where intrinsic curvature is zero along the arc-length and a prescribed load at the tip is absent.

In Fig. 4.8(a) we show several successive rod configurations represented by the the circles on the S-curve in Fig. 4.3 based on the constant 10° iterative change in the value of θ_{tip}. The configurations are solved backward (starting at the X-Y origin) via an IVP using initial conditions at the tip of the rod. In Fig. 4.8(b) we rearrange the solutions in Fig. 4.8(a) so that the base of all the rods meet at the X-Y origin.

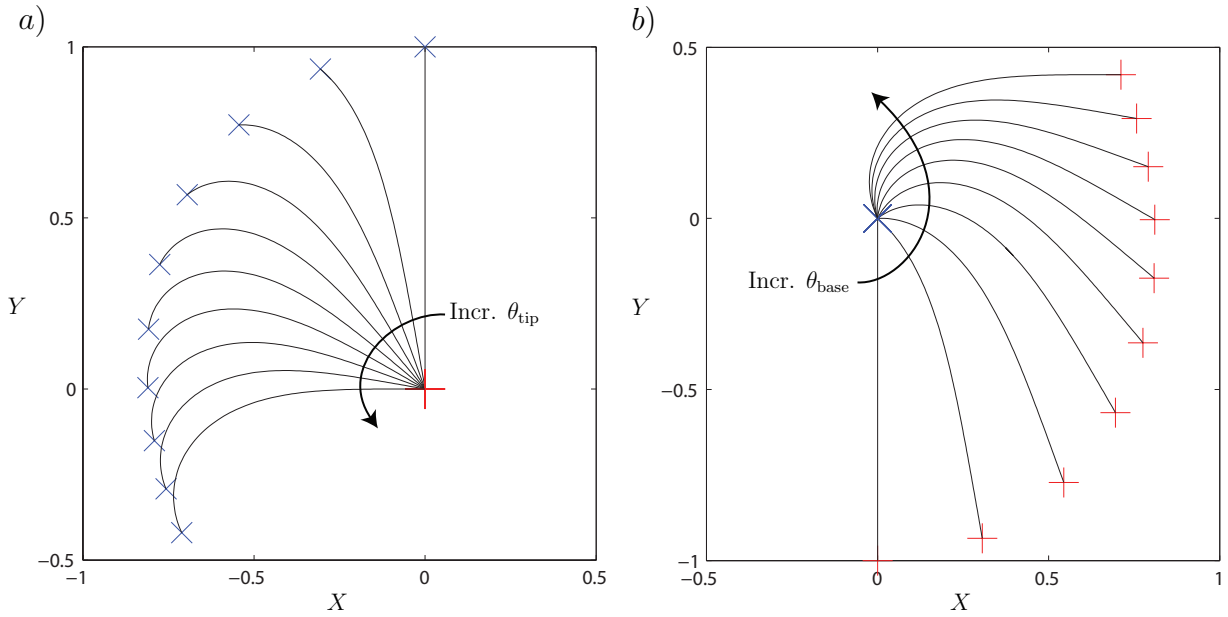

Figure 4.8: *The value of θ_{tip} is varied at 10° intervals between the set $[-90°, 0°]$ with $\alpha = 15$. We recall that there are unstable solutions in the complete family of solutions for this value of α. a) The free tip of any rod is marked by a cross that coincides with the origin, while the base of a rod is marked by an X. b) The free tip of any rod is marked by a cross, while the base of a rod is marked by an X that coincides with the origin.*

A novel physical analogy for the representation in Fig. 4.8(b) is a sheet of paper held at one end by the one's fingertips (see Fig. 4.9). One can trace the same progressive pattern of configurations by starting with the paper dangling straight down and slowly rotating the gripped end of the paper about an axis that is coincident with the paper's horizontal edge. By our physical example we intuitively find that all the solutions in Fig. 4.8(b) are stable.

If one keeps turning the sheet, eventually the sheet jumps to another stable configuration. This phenomenon is captured and indicated on the S-curve by the two jumping

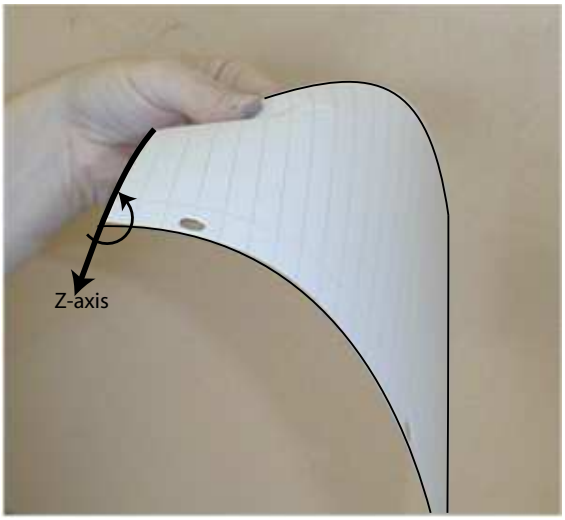

Figure 4.9: *A physical representation of the solutions in Fig. 4.8b can be made by dangling a sheet of paper straight down and then turning the base counter-clockwise about the labeled Z-axis.*

points in Fig. 4.6. We find that once the configuration jumps, a back tracking of the base angle does not return the rod to the previous configuration. Thus, the jumps are one-way transition to a new stable configuration.

With respect to Fig. 4.8, we increase the θ_{tip} interval to $[-90°, 90°]$ and display the results in Fig. 4.10(a). Due to symmetry, mirroring of the solutions in Fig. 4.10(a) about the Y-axis would represent a set of solutions on the θ_{tip} interval $[-90°, 270°]$.

In Fig. 4.10(a) we start with the configuration of a hanging straight rod and turn about the Z-axis at the base. At a certain base angle the value of θ_{base} stops increasing as θ_{tip} increases. We show this transition point in more detail in Fig. 4.10(b). This transition point marks the jumping point between stable configurations and unstable configurations shown in Fig. 4.2. As in the simulation, the paper sheet from our physical example will jump to a new stable configuration when the base angle attains a similar point.

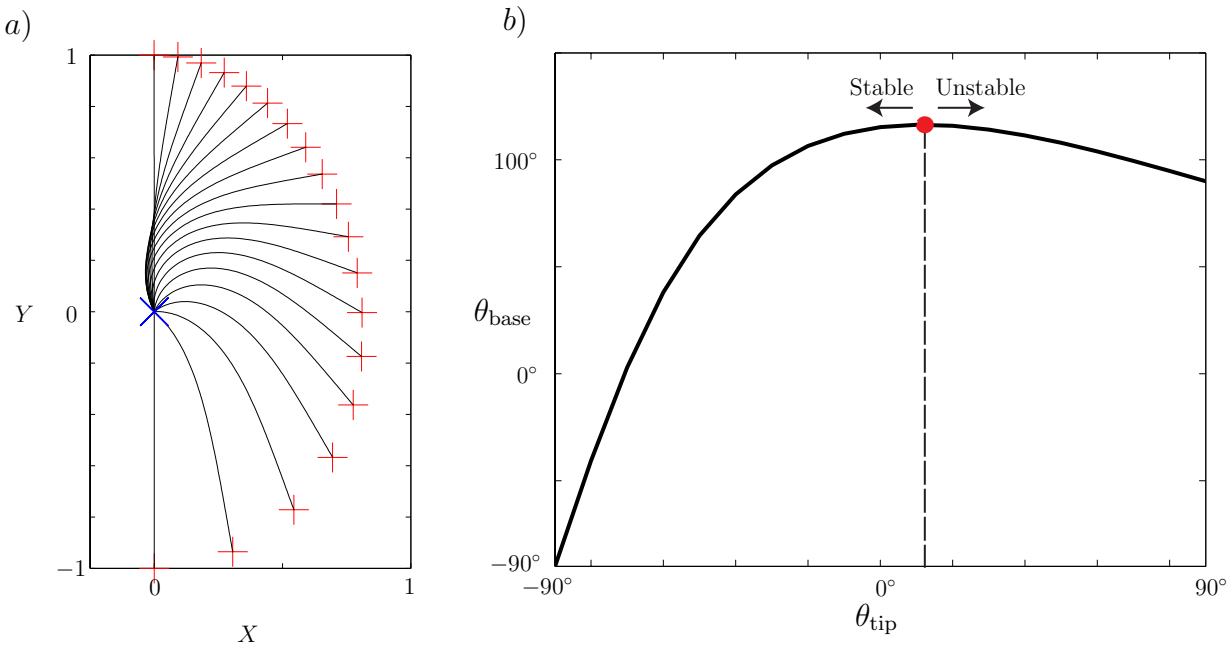

Figure 4.10: *The value of θ_{tip} is varied at $10°$ intervals between the set $[-90°, 90°]$ with $\alpha = 15$. a) The free tip of any rod is marked by a cross, while the base of a rod is marked by an X that coincides with the origin. An additional mirroring of these solutions about the Y-axis would give a complete set of all the potential solutions for this α-configuration and produce a set of solutions on the θ_{tip} interval $[-90°, 270°]$. b) As we move from left to right along the curve we find that there is a point where θ_{base} can no longer increase thus suggesting a point of demarcation between a stable region and unstable region of configurations.*

Chapter 5

Computing the Equilibria of Branched Plant Stems

In this chapter, we use our earlier work from Chapters 2 and 4 to simulate configurations with multiple branches. We do not incorporate the work on growth that we developed in Chapter 3. Indeed, a unifying model for the growth of configurations with multiple branches[1] is left as a subject for future work. However, our method of simulating multiple branches was developed with the intention of simulating growth in the future.

5.1 Using the S-curve for Multiple Branches

As in the case of a single rod, the S-curve is used to isolate a preferred set of branched configurations. This is done by generating individual S-curves for each branch. Beginning at free-end branches, i.e., branches that are the furthest downstream of a single base branch[2], each S-curve of a downstream branch or branches are used to generate an S-curve for a neighboring upstream branch until the base branch is reached (see Fig. 5.1).

Typically, we choose not to impose a singular force $\mathbf{F}$ or singular moment $\mathbf{M}$ at the tip of free-end branches. As a result, the boundary conditions at the extremities of the branched structure are

$$\begin{aligned} \mathbf{F}_1(\theta^1_{\text{tip}}) &= \mathbf{0}, \\ \mathbf{M}_1(\theta^1_{\text{tip}}) &= \mathbf{0}, \end{aligned} \tag{5.1}$$

where θ_{tip} and θ_{base} are angles at the downstream and upstream end of an individual branch, respectively. The indices quantify *branch level* in a branch hierarchy, (cf. Fig. 5.1). Equations $(5.1)_2$ and (2.24) imply that

$$\nu_1(\theta^1_{\text{tip}}) = 0. \tag{5.2}$$

[1]For simplicity, we refer to configurations with multiple branches as *branched configurations*.

[2]Due to *contractive flow*, we assume that all branched configurations terminate upstream at a single base branch.

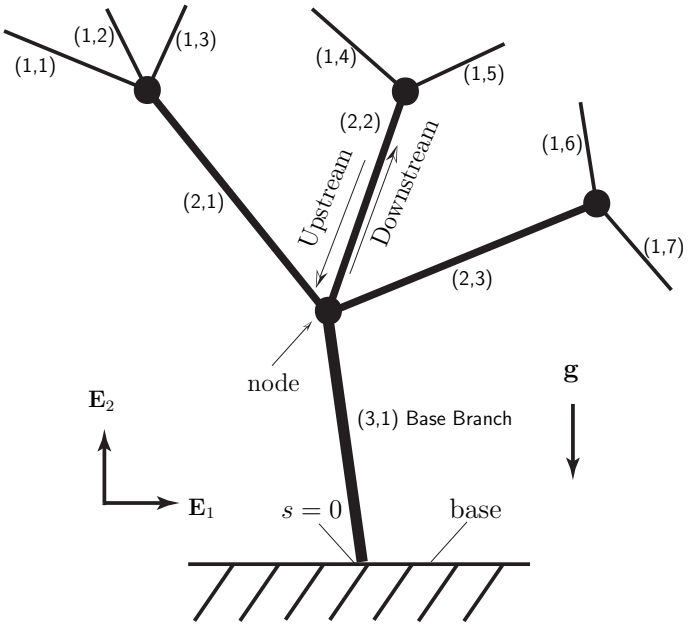

Figure 5.1: *An example of branch hierarchy is shown. More complex tree structures may require a different labeling system. Branches are labeled in parenthesis with two coordinates:* (x, y) *The first coordinate,* x*, is the branch level, where the higher the number, the closer the branch is to the base branch. The second coordinate,* y*, is the individual branch number at a particular branch level.*

The singular force $\mathbf{F}$, singular moment $\mathbf{M}$, and strain ν are functions of θ_{tip}, the variable initial condition that is used to generate an S-curve.

After generating S-curves for the free-end branches, we use the *discontinuity equivalence* developed in Section 2.7.1 and let the branches just upstream of the initial free-end branches become equivalent free-end branches with imposed singular forces $\mathbf{F}_2(\theta^2_{\text{tip}})$ and singular moments $\mathbf{M}_2(\theta^2_{\text{tip}})$. The initial conditions for the strain are developed from the downstream (free-end branch) S-curves and the downstream branch's equations of motion (2.33). The new initial conditions $\nu_2(\theta^2_{\text{tip}})$ are developed from the S-curves downstream of the branch and satisfy the jump condition $(2.22)_2$. The singular force $\mathbf{F}_2$ is generally a constant vertical force and satisfies the jump condition $(2.22)_1$. Relative to two branches at a node (one being an upstream branch and the other being a downstream branch) the following relation between angles holds:

$$\theta^i_{\text{base}} = \theta^{i+1}_{\text{tip}} + \theta_{\text{offset}}, \tag{5.3}$$

where θ_{offset} is the difference between the angles subtended to the vertical by the tangent vectors to the two branches at the node (cf. Fig. 5.2(a)). This iterative process continues until the base branch is reached. A schematic of the process for a base branch with two free-end branches is shown in Fig. 5.2.

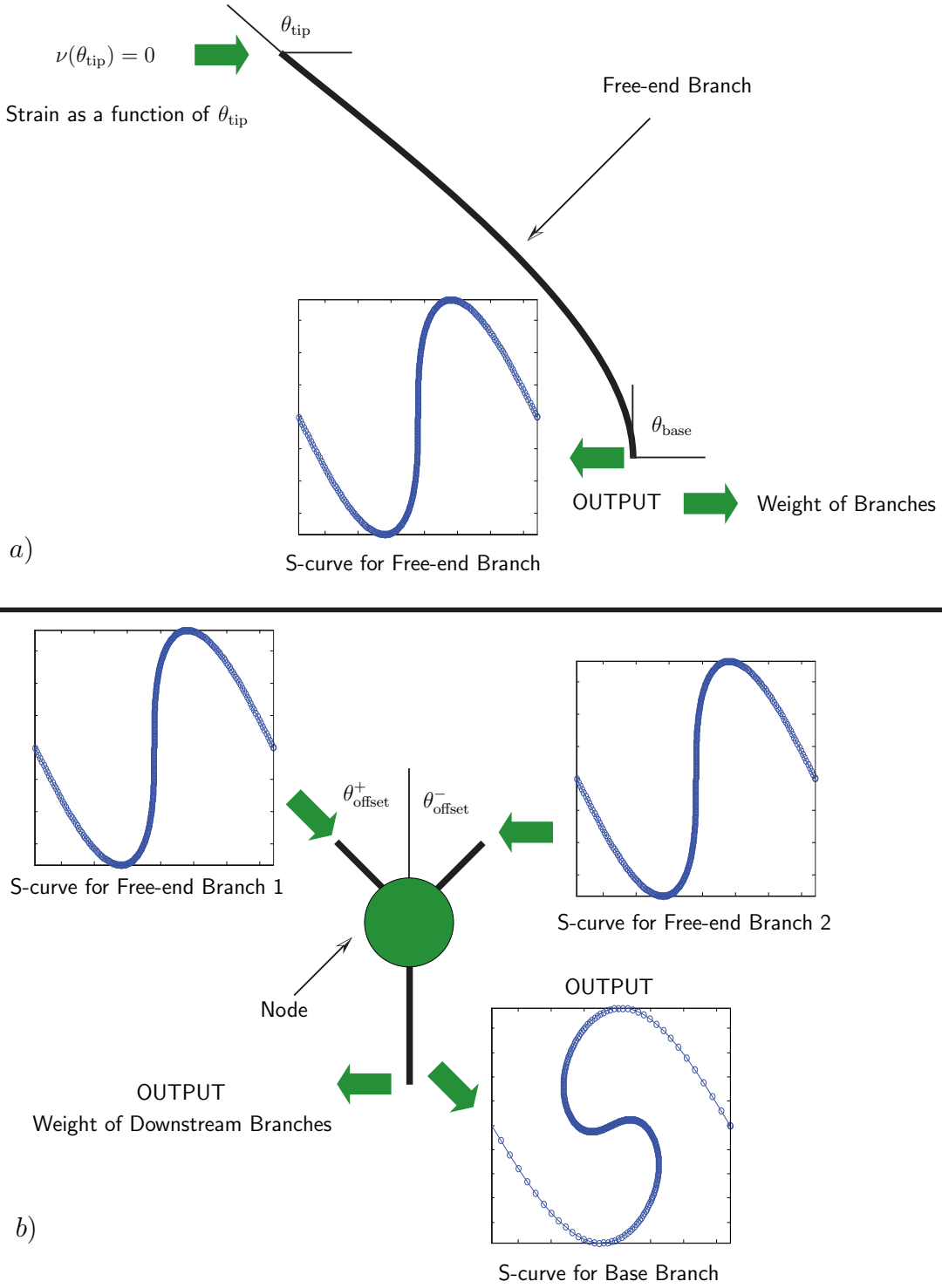

Figure 5.2: *Sending S-curves upstream: For a three-branch configuration, a) the S-curves for free-end branches are generated, b) at the node the S-curves of the free-end branches are combined so that offset angle θ_{offset} is accommodated and the jump condition $(2.22)_2$ is satisfied. This information, along with the combined weight of the free-end branch is used to create an S-curve for the base branch.*

The strain ν is generally a single-valued function of θ_{base}. However, for certain S-curves this is not the case. In this situation, we can construct the S-curve by combining several discontinuous functions. Using the S-curve from Fig. 4.6, an example of this construction is shown in Fig. 5.3. One function is due to an increasing θ_{base} variable, while the other function is due to a decreasing θ_{base} variable.

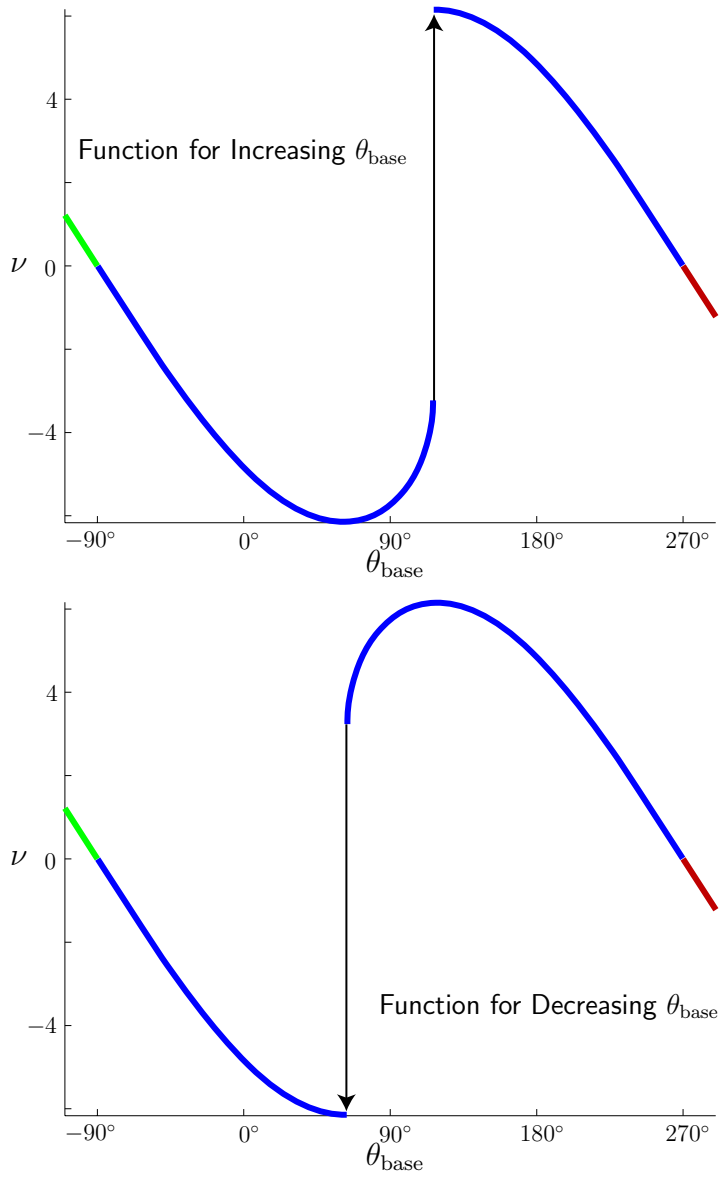

Figure 5.3: *The S-curve from Fig. 4.6 is decomposed into two functions each with a dislocation discontinuity. Each function is sent upstream to form a single S-curve with overlapping segments.*

5.2 Simulating Configurations with Multiple Branches

In Fig. 5.4 we show a simulation of two S-curves representing two free-end branches each with jumping points being compressed into a single S-curve at the node. There are four states when the base branch is vertical. When the tip of the base branch is at 90°, these stable states correspond to: branch 1 leaning left, branch 2 leaning right; branch 1 leaning right, branch 2 leaning left; branch 1 leaning left, branch 2 leaning left; and branch 1 leaning right, branch 2 leaning right. An S-curve is generated for the base branch and is shown in Fig. 5.6. Notice how the four potential solutions for one set of boundary conditions manifests in the S-curve.

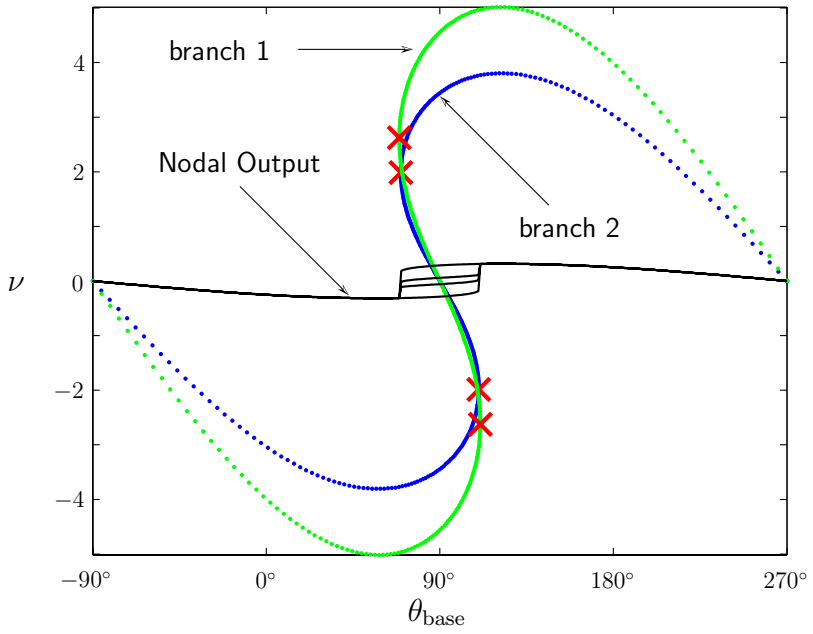

Figure 5.4: *The construction of a composite S-curve for case of two free-end branches connected to a base branch with zero offset angle:* $\theta_{offset} = 0$. *Jumping points are denoted by an* $\times$. *Notice that, close to* $\theta_{base} = 90°$, *there are four steps in this curve representing four possible configurations. Also, the curve is contracted vertically due to the fact that the base is much stiffer than the branches, and thus the strain is much smaller. A scaled figure of the nodal output is shown in Fig. 5.5.*

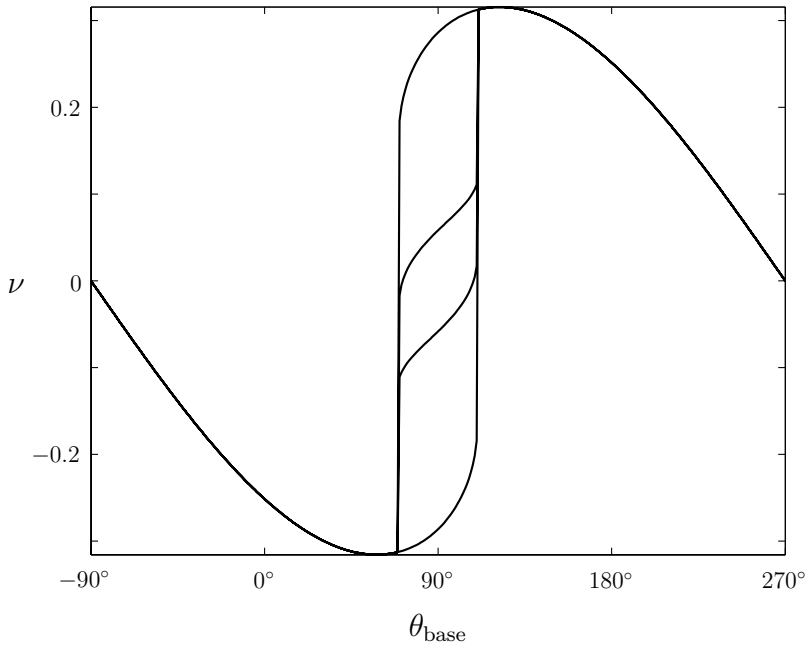

Figure 5.5: *The nodal output (i.e., composite S-curve) from Fig. 5.4.*

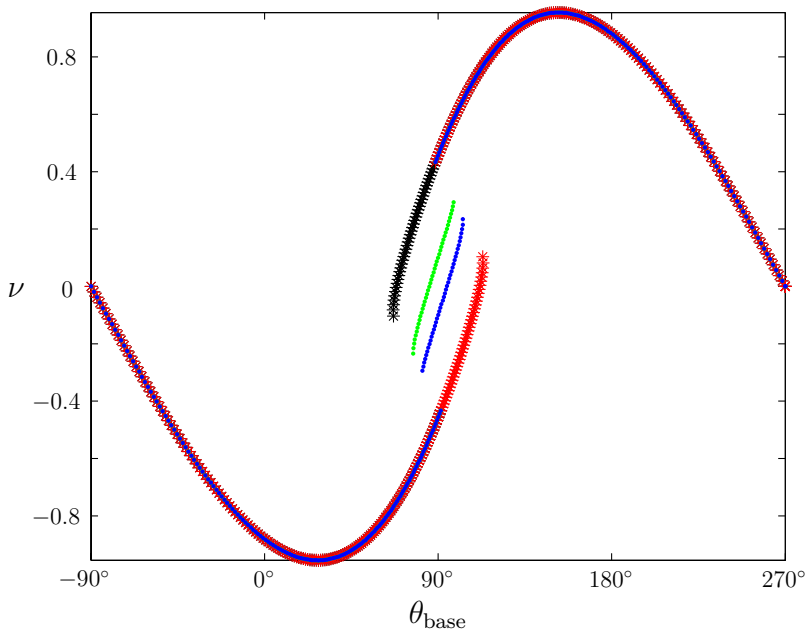

Figure 5.6: *The composite S-curve in Fig. 5.4 is decomposed into four segments, which combine to form the total S-curve of the base branch. Various segments of the partial S-curves overlap to form a complete S-curve.*

5.2.1 Branched System Simulation

We close this chapter with an example illustrating the possible configurations of a complex branched structure. In this case, we consider a base which bifurcates, and each of the resulting branches also bifurcates. As a result, we end up with a plant with 7 branches. The question we seek to address is the static equilibrium configurations of the resulting structure. To find these configurations, we use the S-curve method discussed earlier.

With the help of the S-curve, a range of possible configurations of a (7)-branch configuration are shown in Fig. 5.7. Here, the base angle is increasing in a counter-clockwise manner. The branch tips have a constant intrinsic curvature along the arc-length parameter and there are offset angles for each branch at the nodes. The process of constructing a series of S-curves from the free-end branches down to the base branch allows us to choose the initial conditions of an angle and corresponding strain at the base and integrate out towards the free-end branch tips in order to determine the spatial configuration. Along the way, we use individual branch S-curves to supply us with initial conditions at each node.

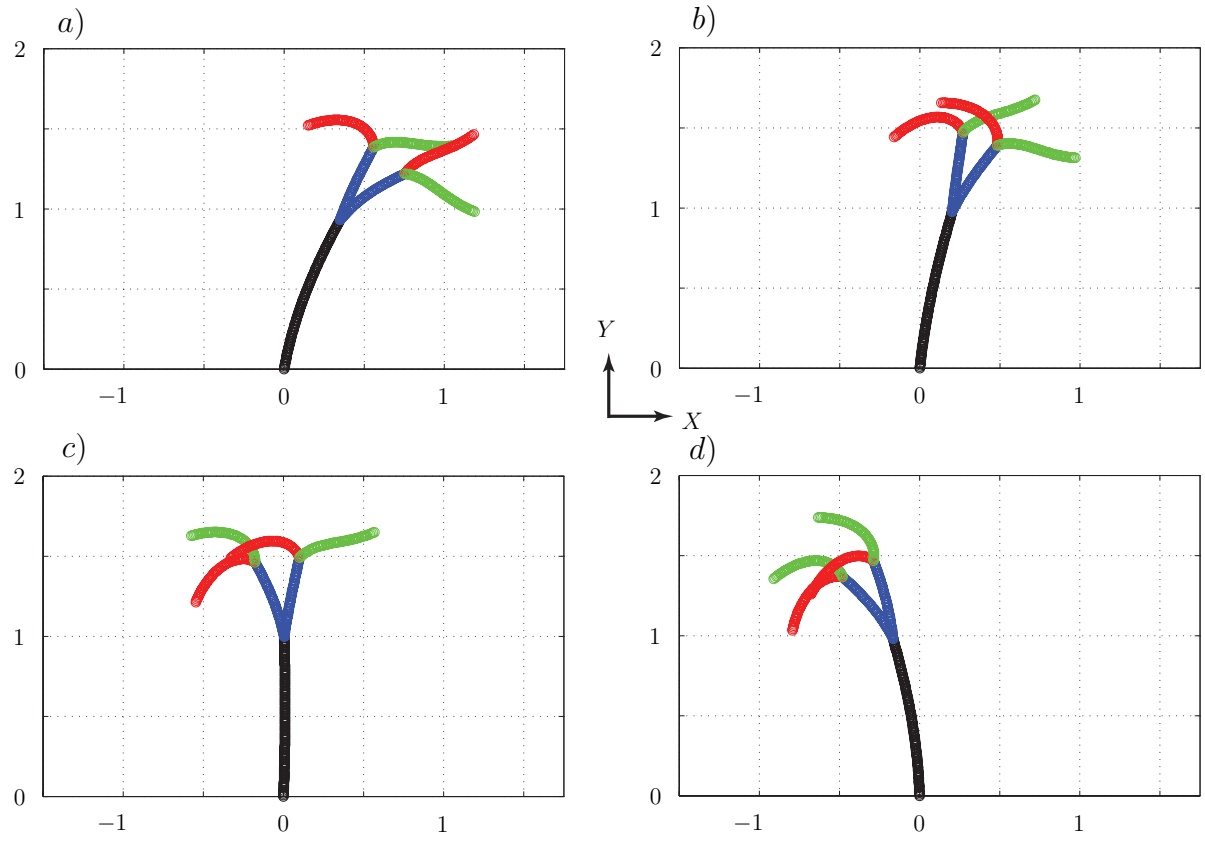

Figure 5.7: *Configurations of a plant with seven branches with a varying base angle. The free-end branches have a constant intrinsic curvature with respect to the arc-length parameter. The base angle for the base branch at each segment is: a)* 80°*; b)* 84°*; c)* 88°*; d)* 92°*.*

Chapter 6

Future Work

The work in this dissertation has established a foundation for further research in areas involving physical experiments and an extension of our current model and theory. Our foremost desire is to strengthen collaboration with botanists and plant biologists in order to begin experiments on a select set of free standing wooden and non-wooden plants. However, before our physical experiments can advance, we must establish a streamline approach that combines the elements of growth developed in Chapter 3 and branching developed in Chapter 5. As we mentioned in Section 3.7, a proper model for decreasing stiffness has also yet to be established. Likewise, we would like to extended our current planar rod theory into a three-dimensional theory.

Working with a botanist, we would like to devise experiments to rigorously test the accuracy of our model. In the same way that Silk et al. [1] chose the rice panicle for her research, we too would begin our physical experiments with plants that embody a simple structure with straightforward constitutive properties. Initial plant experimentation and consultation with a biologist are also essential steps toward the development of control laws, similar to those developed in Chapter 3, that would capture various plant tropisms.

Our current model would also be enhanced by determining how to handle decreasing stiffness. In Section 3.7 we discussed the case of decreasing stiffness for a rod without residual stress and stated that during a uniform softening of the rod, the growth configuration remains constant. However, for a rod under residual stress a change in the stiffness can result in a change in the growth configuration. Recalling the rod in Fig. 3.6, now redisplayed in Fig. 6.1, we notice that if the stiffness of the configuration $\mathcal{L}_1$ softens, then the curvature of the composite configuration $\mathcal{L}_{12}$ would change in such a way as to bend the tip of the configuration $\mathcal{L}_{12}$ upward as the curvature of the configuration $\mathcal{L}_2$ becomes dominant. We have created several prototype models to deal with decreasing stiffness, but further research is required to properly develop these initial models.

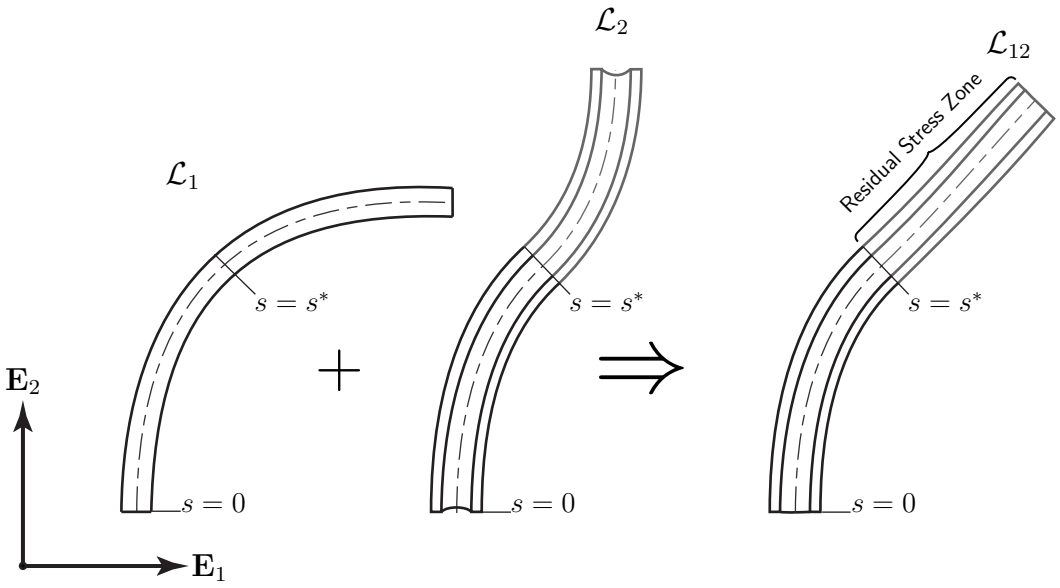

Figure 6.1: *Two rod configurations, $\mathcal{L}_1$ and $\mathcal{L}_2$, are of equal length L and have identical curvature profiles between $s = 0$ and $s = s^*$. The parameter κ^c marks the difference in curvature along the arc-length. These two rods form a composite rod configuration $\mathcal{L}_{12}$, where $\kappa^c = 0$ in $s \in [0, s^*)$ represents a zone with zero residual stress and $\kappa^c \neq 0$ in $s \in [s^*, L]$ is a residually stressed zone.*

The union of growth and branching into one model requires further investigation using numerical methods. Over the course of this work, various numerical problems, involving the transition from theory to simulation, were solved. Most of the numerical issues surrounded the implementation of the S-curve. For example, due to the inherent stretch of the curve, shown in Fig. 4.4, the calculation of the S-curve would slow down tremendously in areas where intervals of θ_{tip}, the variable that parameterizes the S-curve, would yield a relatively small interval of arc-length on the S-curve. An algorithm was devised that increases the size of θ_{tip} intervals in response this particular slow down. A particular unresolved problem is a complication due to growth that occurs when a branch changes its dimensions or constitutive properties. The S-curve of the branch experiencing growth also changes, which causes all of the S-curves of branches upstream to change. Again, there are several prototype algorithms we have devised to combine growth and branching, but more work is needed to develop them.

Finally, we would like to extend out current planar rod theory into a three-dimensional theory for the chief purpose of modeling torsion and properly capturing the spatial configurations of the plants we desire to model. It is unknown to us if the S-curve can be generalized to a three-dimensional model. We do know that if it does exist, the set of preferred configurations the S-curve predicts can be reduced due to the lack of torsional rigidity in the rod.

Bibliography

[1] W. K. Silk, R. O. Erickson, Kinematics of plant growth, Scientific America 242 (5) (1980) 134–151.

[2] M. Yoshida, H. Yamamoto, Growth stress controls negative gravitropism in woody plant stems, Planta 216 (2) (2002) 280–292. doi:10.1007/s00425-002-0846-x.

[3] A. Goriely, S. Neukirch, Mechanics of climbing and attachment in twining plants, Phys. Rev. Lett. 97 (18). doi:10.1103/PhysRevLett.97.184302.

[4] A. H. Brown, Circumnutations: from Darwin to space flights, Plant Physiol. 101 (2) (1993) 345348.

[5] W. Kurth, Morphological models of plant growth: Possibilities and ecological relevance, Ecological Modelling 75 (76) (1994) 299–308. doi:10.1016/0304-3800(94)90027-2.

[6] W. Silk, L. Wang, R. Cleland, Mechanical properties of the rice panicle, Plant Physiol 70 (2) (1982) 460–464.
URL `http://www.plantphysiol.org/cgi/content/abstract/70/2/460`

[7] T. McMillen, A. Goriely, Tendril perversion in intrinsically curved rods, Journal of Nonlinear Science 12 (3) (2002) 241–281. doi:10.1007/s00332-002-0493-1.

[8] A. Goriely, M. Robertson-Tessi, M. Tabor, R. Vandiver, Elastic growth models, Vol. 102, Springer Berlin Heidelberg, Berlin, 2008, pp. 1–44.

[9] N. A. Faruk Senan, O. M. O'Reilly, T. N. Tresierras, Modeling the growth and branching of plants: A simple rod-based model, J. Mech. Phys. Solids 56 (10) (2008) 3021–3036. doi:10.1016/j.jmps.2008.06.005.

[10] A. Goriely, R. E. Goldstein, Dynamic buckling of morphoelastic filaments, Phys. Rev. E. 74 (1). doi:10.1103/PhysRevE.74.010901.

[11] S. Antman, Nonlinear Problems of Elasticity, Springer-Verlag, New York, 1995.

[12] S. S. Antman, Kirchhoff's problem for nonlinearly elastic rods, Q. Appl. Math. 32 (1974) 221–240.

[13] A. E. Green, P. M. Naghdi, A unified procedure for construction of theories of deformable media. II. Generalized continua, Proc. Roy. Soc. London Ser. A 448 (1934) (1995) 357–377.

[14] M. B. Rubin, Cosserat Theories: Shells, Rods, and Points, Kluwer Academic Press, Dordrecht, 2000.

[15] A. E. H. Love, A Treatise on the Mathematical Theory of Elasticity, Dover Publications, Inc., New York, 1944.

[16] A. Green, P. Naghdi, On thermal effects in the theory of rods, International Journal of Solids and Structures 15 (11) (1979) 829–853.

[17] Hangarter, Brief history of the discovery of plant hormones:auxin, polar auxin transport and tropisms, http://www.bio.indiana.edu/ hangarter-lab/courses/b373/lecturenotes/tropisms/tropism2.html.

[18] F. S. Malan, Eucalyptus improvement for lumber production, in: Proceedings of IUFRO Conference, International Workshop on Utilization of Eucalypts, San Paulo, Brazil, 1995, pp. 1–19.

[19] A. Hoger, On the determination of residual stress in an elastic body, Ecological Modelling 16 (3) (1986) 303–324. doi:10.1007/BF00040818.

[20] L. Euler, Determinatio onerum, quae columnae gesture valent, Vol. 17 of series 2, Orell Füssli Turici, Switzerland, 1982, pp. 232–251.

[21] L. Euler, Examen insignis paradoxi in theoria columnarum occurentis, Vol. 17 of series 2, Orell Füssli Turici, Switzerland, 1982, pp. 252–265.

[22] J. B. Keller, The shape of the strongest column, Arch. Rat. Mech. Anal. 5 (1960) 275–285.

[23] J. B. Keller, F. I. Niordson, The tallest column, J. Math. Mech. 16 (1966) 433–446.

[24] S. J. Cox, C. M. McCarthy, The shape of the tallest column, SIAM J. Math. Anal. 29 (3) (1998) 433–446.

[25] J. Neu, Y. Farjoun, The tallest column a dynamical system approach using a symmetry solution, Studies in Applied Mathematics 115 (2005) 319–337.
URL `http://arxiv.org/abs/0711.0730v2`

[26] M. Yoshida, T. Okuyama, Techniques for measuring growth stress on the xylem surface using strain and dial gauges, Holzforschung 56 (5) (2002) 461–467. doi:10.1515/HF.2002.071.

[27] C. Fox, An Introduction to the Calculus of Variations, Dover, New York, 1963.

[28] A. Green, N. Laws, Remarks on the theory of rods, Journal of Elasticity 3 (1973) 179–184.

[29] O. M. O'Reilly, The energy jump condition for thermomechanical media in the presence of configurational forces, Continuum Mechanics and Thermodynamics 18 (6) (2006) 361–365. doi:10.1007/s00161-006-0036-3.

[30] A. Green, P. Naghdi, M. Wenner, On the theory of rods: Ii. developments by direct approach, Proceedings of the Royal Society of London 337 (1611) (1974) 485–507. URL http://www.jstor.org/stable/78527

[31] O. M. O'Reilly, On steady motions of a drawn cable, J. Appl. Mech 63 (1) (1996) 180–189. doi:10.1115/1.2787196.

Appendix A

The Equations of Motion for the Elastica from a Variational Principle

It is well-known that the equations of motion for the elastica (2.33) can be derived from a variational principle. Specifically, once the energy functional for the branching rod is prescribed,

$$V = \int_0^L F(\theta, \theta') \mathrm{d}s, \tag{A.1}$$

then the equations of motion are determined from the Euler Lagrange equation:

$$\frac{\mathrm{d}}{\mathrm{d}s}\left(\frac{\partial F(\theta, \theta')}{\partial \theta'}\right) - \frac{\partial F(\theta, \theta')}{\partial \theta} = 0. \tag{A.2}$$

In this appendix, we outline the procedure for prescribing V and showing how it results in the equations of motion (2.33). The resulting V is a component in the construction of the S-curves.

The proposed functional $F$is a sum of the strain energy, self-weight potential energy, and vertical load potential at the tip of the rod. For free tip branches, this load potential is zero. In words, the functional is expressed as

$$V = \text{Strain Energy} + \text{Distributed Potential Engery} + \text{Singular Potential Energy}.$$

That is,

$$V = \int_0^L \left[\frac{1}{2} D(s)(\theta' - \kappa^g(s))^2 + \rho(s) g z(s) + W \sin(\theta)\right] \mathrm{d}s, \tag{A.3}$$

where κ^g is intrinsic strain, $z(s)$ is vertical height at s, $\rho(s)$ is the density per unit length, and W is a constant vertical load at the tip of the rod. The expression for $z(s)$ is

$$z(s) = \int_0^s \sin(\theta(t)) \mathrm{d}t. \tag{A.4}$$

Likewise, the height of the load, W, is

$$\int_0^L \sin(\theta(t)) \mathrm{d}t. \tag{A.5}$$

To show the compatibility of V with the equations of motion, we first note that the general change of order of integration for the following bounds is[1]

$$\int_0^L \int_0^s f(x,s)\mathrm{d}x\mathrm{d}s = \int_0^L \int_s^L f(x,s)\mathrm{d}s\mathrm{d}x. \tag{A.6}$$

Equation (A.3) can be rearranged using the following sequence of steps:

$$\begin{aligned}
V &= \int_0^L \left[\frac{1}{2}D(s)(\theta' - \kappa^g(s))^2 + \rho(s)g\int_0^s \sin(\theta(x))\ \mathrm{d}x + W\sin(\theta)\right]\mathrm{d}s \\
&= \int_0^L \frac{1}{2}D(s)(\theta' - \kappa^g(s))^2\ \mathrm{d}s + g\int_0^L\int_0^s \rho(s)\sin(\theta(x))\ \mathrm{d}x\mathrm{d}s + \int_0^L W\sin(\theta)\ \mathrm{d}s \\
&= \int_0^L \frac{1}{2}D(s)(\theta' - \kappa^g(s))^2\ \mathrm{d}s + g\int_0^L\int_s^L \rho(s)\sin(\theta(x))\ \mathrm{d}s\mathrm{d}x + \int_0^L W\sin(\theta)\ \mathrm{d}s \\
&= \int_0^L \frac{1}{2}D(s)(\theta' - \kappa^g(s))^2\ \mathrm{d}s + g\int_0^L \sin(\theta(x))\int_s^L \rho(s)\ \mathrm{d}s\mathrm{d}x + \int_0^L W\sin(\theta)\ \mathrm{d}s \\
&= \int_0^L \left[\frac{1}{2}D(s)(\theta' - \kappa^g(s))^2 + g\sin(\theta(s))\int_s^L \rho(x)\ \mathrm{d}x + W\sin(\theta)\right]\mathrm{d}s \\
&= \int_0^L \left[\frac{1}{2}D(s)(\theta' - \kappa^g(s))^2 + g\sin(\theta(s))\int_L^s -\rho(x)\ \mathrm{d}x + W\sin(\theta)\right]\mathrm{d}s.
\end{aligned} \tag{A.7}$$

Now, $F(\theta,\theta')$ is

$$F = \frac{1}{2}D(s)(\theta' - \kappa^g(s))^2 + g\sin(\theta)\int_L^s -\rho(x)\ \mathrm{d}x + W\sin(\theta). \tag{A.8}$$

If we now define the integral,

$$\mathcal{P} = \int_L^s -\rho(x)\ \mathrm{d}x, \tag{A.9}$$

then the previous expression for F simplifies to

$$F = \frac{1}{2}D(s)(\theta' - \kappa^g(s))^2 + \mathcal{P}(s)g\sin(\theta) + W\sin(\theta). \tag{A.10}$$

Substituting $F(\theta,\theta')$ into the Euler-Lagrange equation and using the definition for ν gives

$$D'(s)\nu + D(s)\nu' - (\mathcal{P}(s)g + W)\cos(\theta) = 0. \tag{A.11}$$

This is the general equation for equilibrium of a branch (which can be a part of a larger branched system). Solving for ν and letting $W = n_l$ we arrive at the equations (2.33).

[1] In (A.6), the arc-length parameter s is a variable of the integral and the bounds.